

Nanoporous noble metals by alloy corrosion: formation process, microstructure and surface- stress-charge behaviors

Dissertation
zur Erlangung des Grades
des Doktors der Ingenieurwissenschaften
der Naturwissenschaftlich-Technischen Fakultät II
– Physik und Mechatronik –
der Universität des Saarlandes

Von

Smrutiranjana Parida

Saarbrücken

2007

Tag des Kolloquiums:	13.12.2007
Dekanin/Dekan:	Univ.-Prof. Dr. Andreas Schütze
Mitglieder des Prüfungsausschusses:	Priv.-Doz. Dr. Jörg Weißmüller Univ.-Prof. Dr. Rolf Pelster Univ.-Prof. Dr. Ludger Santen
Akademische Mitarbeiterin/ Akademischer Mitarbeiter	Dr. Patrick Huber

Zusammenfassung / Abstract

Nanoporöse Edelmetalle durch Legierungsauflösung: Herstellungsprozess, Mikrostruktur und Oberflächenladungsverhalten

Das Ziel dieser Studie ist die Untersuchung folgender Aspekte nanoporöser Goldstrukturen, die durch Legierungsauflösung hergestellt wurden: a) Zusammenhänge zwischen Herstellungsprozeß, Mikrostruktur und Eigenschaften, b) Untersuchung der Auswirkung der Auflösungsrate, Strukturgröße und Defektbildung in der Mikrostruktur auf den Volumenschrumpf während der Legierungsauflösung, c) Bestimmung der physikalischen Eigenschaften einer dreidimensionalen zweifach zusammenhängender nanoporöser Morphologie, d) Stabilisierung der porösen Mikrostruktur durch Zugabe von Pt, e) die Korrelation zwischen der Amplitude der oberflächenspannungsinduzierten Dehnung und der Größe der Längenskala in den nanoporösen Strukturen, die durch Legierungsauflösung hergestellt wurden, f) Untersuchung des Einflusses von Adsorbatbedeckung auf die Reaktion der Oberflächenspannung auf der Metalloberfläche an der nanoporösen Metall-Elektrolyt Grenzfläche. Erstmals wurde ein Volumenschrumpf während der Legierungsauflösung in Au-Ag Legierungen beobachtet, der nicht mit dem gängigen Modell der Legierungsauflösung, welches auf Oberflächendiffusion basiert, erklärt werden kann. Ebenfalls erstmalig wurde eine Z-Kontrast-Tomographie an nanoporösen Metallen durchgeführt, um die ihnen innewohnende dreidimensionale Morphologie zu visualisieren.

Nanoporous noble metals by alloy corrosion: formation process, microstructure and surface-stress-charge behaviors

This work attempts to explore following aspects of nanoporous noble metal and alloys structures prepared by dealloying: a) inter-relation between formation process, microstructure and property, b) study of the effect of dealloying rate, structure size and defect generation in the microstructure on the volume shrinkage during dealloying, c) determination of the physical properties of the three dimensional bi-continuous nanoporous morphology, d) stabilization of porous microstructure by Pt addition, e) the correlation between amplitude of the surface-stress-induced strain and size of the length scale in nanoporous structures prepared by dealloying, f) study of the effect of adsorbate coverage on the surface-stress-charge response of the metal surface at nanoporous metal-electrolyte interface. For the first time, volume shrinkage during dealloying was reported in Au-Ag alloys, which is not consistent with the present model of dealloying based on surface diffusion. For the first time, Z-contrast tomography was carried out on nanoporous metals prepared by dealloying to visualize it inherent in three dimension morphology.

Zusammenfassung

Die vorliegende Arbeit zielt darauf, die folgenden Aspekte nanoporöser Edelmetalle und Legierungen, die mit der Legierungsauflösung hergestellt wurden, zu erforschen: a) Strukturaufklärung und Bestimmung der physikalischen Eigenschaften der dreidimensionalen, bikontinuierlichen und nanoporösen Strukturen, b) der Zusammenhang zwischen der Legierungsauflösungsgeschwindigkeit, der Strukturgröße und der Entstehung von Defekten, c) der Einfluss einer Oxidationsschicht auf die Reaktion der elastischen Grenzflächenspannung auf die Ladung der Phasengrenze Metallelektrode-Elektrolyt, und d) die Beziehung zwischen der durch die elastischen Grenzflächenspannung hervorgerufene Dehnungsamplitude und der Strukturgröße in den nanoporösen Gefügen, die durch Legierungsauflösung erhalten wurden.

Die strukturellen und funktionellen Eigenschaften der Legierungsauflösungsstrukturen hängen von ihrer Morphologie ab: Eine vollständige Beschreibung der Mikrostruktur und der Topologie der nanoporösen Gebilde schließt die Bestimmung der Verteilung der Poren- und Steggrößen ein, der Verbindungen innerhalb der Poren und innerhalb der Stege, der spezifischen Oberfläche und der mittleren Krümmung der Mikrostruktur. Erstmals wurde mit nanoporösem Gold als Modellsubstanz und mit Hilfe der dreidimensionalen Elektronentomographie im Durchstrahlungsmikroskop eine ausführliche Beschreibung der zuvor beschriebenen Merkmale für Legierungsauflösungsstrukturen ausgeführt.

Mit Silber-Gold-Legierungen als Modellsystem wurde gezeigt, dass die Geschwindigkeit der Legierungsauflösung die makroskopischen Abmessungen der Probe beeinflusst, die Poren- und Stegabmessungen und die Defektdichte in der Mikrostruktur. Erstmals wurde eine makroskopische Volumenreduktion der Probe von bis zu 20% während der elektrochemischen Legierungsauflösung von Edelmetallegierungen beobachtet. Die Röntgen- und Texturmessungen zeigen, dass die Kornstruktur der ursprünglichen Ausgangslegierung während der Auflösung beibehalten wird. Daher ist dieses Schrumpfen des Volumens nicht mit einem Vorgang verträglich, der ausschließlich auf Auflösung und diffusiver Bewegung auf den Plätzen eines starren Gitters beruht, wie das gegenwärtige Modell der Legierungsauflösung vorschlägt. Diese Vorgänge auf einem starren Gitter würde die Kornstruktur unverändert lassen, wie in dieser Arbeit auch beobachtet, aber auch die Probenabmessungen. Um die Volumenreduktion zu erklären, haben wir eine Erweiterung des bestehenden Modells vorgeschlagen, das lokale plastische Verformungsprozesse und Defekte in der Mikrostruktur einschließt.

Wenn nanoporöse Metalle in einem Elektrolyten elektrisch aufgeladen werden, dehnen sie sich bei positiveren Potentialen aus und ziehen sich bei negativeren Potentialen zusammen. Dieser Effekt ist eine Folge von Änderungen der elastischen Grenzflächenspannung. Diese ändert sich, wenn etwa eine Änderung der Elektronendichte die Bindungen der Oberflächenatome verändert. Es wurde beobachtet, dass eine Oxidbedeckung, sogar von lediglich einer Monolage, auf der Metalloberfläche ihr ladungsabhängiges Dehnungsverhalten mit der normalen Reaktion der adsorbatfreien Oberfläche, die sich bei positiveren Potentialen ausdehnt und bei negativeren zusammenzieht, ins Gegenteil verkehrt. Weil die Bildung einer massiven Goldoxidschicht während der Legierungsauflösung oder eine Oberflächenrekonstruktion das ungewöhnliche ladungsabhängige Dehnungsverhalten nicht erklären kann, wird eine unvollständige Abschirmung durch eine Oxidschicht vorgeschlagen. Eine Oberflächenoxidschicht verursacht eine tiefere Raumladungszone, in der die Exzessladung, die der Metalloberfläche aufgebracht wird, die volumenartigen unbesetzten Zustände besetzt und dadurch das ungewöhnliche ladungsabhängige Dehnungsverhalten verursacht.

Die Amplitude der durch die elastische Grenzflächenspannung hervorgerufenen Volumendehnung und –Kontraktion von nanoporösen Metallen und Legierungen hängt von der Längenskala der nanoporösen Strukturen ab. Messungen an nanoporösen Gold-Platin-Legierungen, die mit der Legierungsauflösung hergestellt wurden, zeigen einen Anstieg der Dehnungsamplitude mit ansteigendem Platingehalt. Die Beziehung zwischen der Strukturgröße und der Dehnungsamplitude wurde für verschiedene Au-Pt-Legierungen untersucht. Die elektrochemisch bestimmte Oberfläche stieg demnach mit dem Platingehalt der Legierungen an, was nahe legt, dass umso kleinere Poren und Stege entstehen, je größer der Platingehalt der Legierung ist, und dass die Dehnungsamplitude – wie beobachtet – dementsprechend ansteigt. Die maximale Dehnungsamplitude in nanoporösen Au-Pt-Legierungen ist 5-7 mal größer als die von nanoporösem Gold, das durch Legierungsauflösung von Silber-Gold-Legierungen hergestellt wurde.

Acknowledgements

It is a pleasure to thank the many people who made this thesis possible.

It is difficult to overstate my gratitude to my Ph.D. supervisor, PD. Dr. Joerg Weissmueller. With his enthusiasm, his inspiration, and his great efforts to explain things clearly and simply, he helped to make research fun for me. Throughout my research, he provided encouragement, sound advice, good teaching, good company, and lots of good ideas. I heartily thank him for being so kind to me and keeping his door open every time I come to him for help and suggestion. He has helped me develop my professional skills and I will emulate his work ethics throughout my career as a scientist.

I wish to thank my group colleagues Dr. Dominik Kramer and Dr. R.N.Viswanath for their experiences and encouragements during my research at Institute for Nanotechnology.

I gratefully acknowledge the help of Dr. Herald Roesner in obtaining professional TEM micrographs of my samples. I am thankful to Dr. Synthia Volkert for her help in doing FIB measurements. Dr K. Schladitz at Fraunhofer Institut für Techno- und Wirtschaftsmathematik (IFWM), Kaiserslautern, Germany, is thanked for discussions and the stereological analysis using MAVI. Dr C. Kübel at Fraunhofer Institute for Manufacturing Technology and Applied Materials Research (IFAM), Bremen, is thanked for valuable discussions regarding the 3-D reconstructions using Inspect 3D and Amira.

I acknowledge my thankfulness to all my friends and colleagues at Institute for Nanotechnology, for making my stay pleasurable.

I acknowledge the support Christine Batsch, Erika Schütze and Dr. Olaf Wollersheim for taking care of official matters during my whole period of stay at Institute for Nanotechnology.

Financial support from the Deutsche Forschungsgemeinschaft (Centre for Functional Nanostructures Karlsruhe) is gratefully acknowledged.

Contents

Chapter 1: Introduction	1
Reference	4
Chapter 2: Background	6
2.1 Dealloying route to nanoporous metals and alloys	6
2.1.1 Criteria of dealloying	7
2.1.1.1 Thermodynamics	7
2.1.1.2 Composition	7
2.1.1.3 Critical potential	8
2.1.2 Overview of dealloying mechanisms	8
2.1.3 Comparison of dealloying to other electrochemical methods	10
2.2 Charge-induced strain in nanoporous metals and alloys	10
Reference	12
Chapter 3: Materials and methods	13
3.1 Preparation of nanoporous gold (npg) and nanoporous AuPt alloys	14
3.2 In situ strain measurements during dealloying	15
3.2.1 For bulk $\text{Ag}_{75}\text{Au}_{25}$ and $\text{Ag}_{1-x-y}\text{Au}_x\text{Pt}_y$ alloys	15
3.2.2 For gold leaf samples	16
3.3 Reversible strain measurements in nanoporous Au and AuPt alloys	16
3.4 Transmission electron microscopy of npg	17
3.5 Z-contrast tomography	17
3.5.1 Acquisition of tilt series of 2-D projections	18
3.5.2 Reconstruction of 3D image from the data stack	18
3.6 Stereological analysis of tomography of npg	18
3.7 X-ray diffraction and texture measurement	19
3.8 Data processing	19
Reference	20
Chapter 4: Characterization of the microstructure	21
4.1 Introduction	21
4.2 X-ray diffraction of npg	22
4.3 TEM micrographs of npg	24
4.4 3-D reconstruction of npg	25
4.5 Stereological analysis	30
4.5.1 Porosity	30
4.5.2 Ligament- and pore size distributions	30
4.5.3 Net specific surface area	31
4.5.4 Surface orientation distribution	32
4.5.5 Mean curvature	32
4.6 Conclusion	33
Reference	33

Chapter 5: Self-deformation: Effect of the dealloying rate	35
5.1 Introduction	35
5.2 Results	36
5.2.1 Insitu dealloying of $Ag_{1-x}Au_x$ alloys	36
5.2.2 Extent of dealloying shrinkage vs. rate of dealloying	37
5.2.3 E_D and defect in microstructure: TEM observations	38
5.2.4 Dealloying shrinkage vs. composition: Pt addition	41
5.2.5 Shrinkage during electroless dealloying	41
5.3 Discussion and conclusion	42
Reference	44
Chapter 6: Adsorbate effects on the surface-stress-charge response and surface stress-induced strain in npg electrodes	45
6.1 Adsorbate effects on the surface-stress-charge response of npg electrodes	45
6.1.1 Strategy of the experiment	46
6.1.2 Results of <i>Experiment 1</i>	47
6.1.2.1 Strain-charge response in state-I	47
6.1.2.2 Cathodic potential sweep and extent of adsorbate coverage	47
6.1.2.3 Strain-charge response in state-II	49
6.1.2.4 Coarsening after cathodic potential sweep	49
6.1.3 Results of <i>Experiment 2</i>	51
6.1.4 X-ray diffraction experiment	52
6.1.5 Discussion	53
6.2 Enhancing the magnitude of the surface stress-induced strain in npg	55
Reference	58
Chapter 7: Summary	59

Chapter 1: Introduction

Porous materials basically consist of a solid skeleton (of metal, semiconductor, polymer or ceramics) interspersed with pores or voids. Such architecture imparts the material high specific surface area and low specific weight which qualify them for many applications. Desired functional and structural applications of these materials depend on the distribution of sizes, shapes and volumes of the pore spaces and on the chemical nature and size scale of the solid skeleton. Traditional applications of porous materials involve the use of zeolites in ion exchange, adsorption (for separation) and catalysis applications. In past decade, there has been significant advancements in the synthesis methods to fabricate new porous solids with tunable microstructure from a wide range of different materials. This has resulted in porous materials with unusual properties and broadened their application range beyond the traditional use as catalysts and adsorbents.

Because of good permeability, porous metals can be used as filters of gasses and liquids, such as porous Ni-Cr-Al alloy [1] used as filter for the automobile exhaust and use of porous nickel as filter for abstraction of UF_6 . The porous nickel pipe is used to aerate beer, and the porous plate of stainless steel or titanium is used to uniformly oxygenate blood by medical oxygenators. Porous metals can also be used as shock resistance and silencer, electromagnetic shielding, heat exchanger [2]. Porous Ni [3] and porous Cu are used as porous electrode materials, besides their unique application as catalyst and reaction matrix. The interest in nanoporous gold (npg) and nanoporous Au-Pt alloys (covered in this work) is motivated by the prospect of applying the material as a heat exchanger [4], actuator [5,6], sensors [7,8] or as a precursor for producing bulk nanocrystalline gold [9], besides their applications as catalyst [10] and electrocatalyst in fuel cell [11].

Recent research in porous semiconductors is motivated by their optoelectronics, direct band gap semiconductors [12,13] and photonic [14] applications. Besides, these materials provide suitable host materials for fundamental studies in mesoscale confinement. For example, investigation of various types of phase transitions in mesoporous Si, such as the vapour-liquid (capillary condensation), the vapour-solid (capillary sublimation), the liquid-solid (freezing and melting) and some solid-solid transformations [15,16,17].

Several methods of preparation of metallic nanoporous materials include powder metallurgy methods like loose powder sintering and slurry forming [18,19,20], metal deposition e.g. sputter deposition and electro-deposition [21], vacuum evaporation followed by compaction [22], template synthesis using anodized alumina [23], liquid crystal or colloidal templates [24]. Some of these techniques provide poor control over size and extent of porosity, while in other methods, though there is control over these parameters, only porous metals in the form of thin films can be prepared which have insufficient mechanical stability.

Of the several electrochemical methods, dealloying or selective dissolution addresses all these issues in preparation of nanoporous metals. Dealloying offers flexibility to prepare nanoporous metals of different dimension e.g. thin sheet or bulk samples, and the control of porosity and size, besides being economical.

The process of dealloying involves selective removal of one component from a binary or ternary solid solution, resulting in a morphology consisting of bicontinuous metal phase of the remaining element(s) and void phase. Dealloying can be carried out either by application of a suitable potential in an electrochemical cell or in a strong oxidizing medium. By varying dealloying conditions or by post-dealloying treatments, it is possible to prepare nanoporous structures of different length scale. For example, dealloying potentiostatically produces nanoporous metals and alloys with pore size as small as 3-4 nm [25], varying the dealloying time can produce pores as big as 50-60nm. Even bigger pore size can also be produced by post-dealloying heat treatments.

Potential applications of nanoporous metals and alloys in various fields of science and technology, as discussed before, and the interest in studying the dealloying mechanism, has provided great deal of motivation for study of dealloying in various systems such as Ag-Au [26,27], Ni-Au [28], Cu-Pt [24], Cu-Au [29], Au-Cd [30] and Cd-Mg [31] etc.

Being an emerging route to prepare nanoporous metals and alloys, there are several issues in dealloying, which still deserve a closer look, such as: understanding the physical basis of evolution of nanoporosity during dealloying, visualization of the bicontinuous structure formed and studying its nature and physical properties, and the study of defect generation during dealloying. Some of these open issues, which motivated the present study will now be discussed.

An understanding of the dealloying process is necessary to discern the parameters that govern the final structure size in the nanoporous body. The current understanding of dealloying process suggests a diffusive rearrangement of the nobler element (s) in the solid solution, after the removal of the less noble element. Such a rearrangement on a rigid lattice would neither change the original crystal lattice nor would change the overall dimension of the sample. But the observations of dimension change during dealloying [32,33,34] suggest occurrence of other processes during dealloying, besides surface diffusion of nobler component. Study of defect generation during dealloying is one of such issues that need to be studied.

The mean curvature of microstructure of nanoporous metals is an important parameter. Gradients in the mean curvature provide driving forces for transport of matter that leads to coarsening of nanoporous metals. The mean curvature is also important for the local value of the normal component of the surface-induced stress underneath the surface of the ligaments [35]. Measurement of this parameter in nanoporous metals is, therefore, of fundamental interest.

The microstructure of dealloyed structures is of key importance in many engineering applications. Conventional electron microscopy study of nanoporous structures provides insufficient information about its inherently three-dimensional microstructure. Many of the microstructural features of nanoporous materials are always smeared when they are projected into 2-D, as it happens in a SEM or TEM micrograph. So that, many of the physical properties of nanoporous microstructure such as pore shape, size and distribution, ligament connectivity, surface area and mean curvature of the microstructure can not be studied from a SEM or TEM micrograph. This necessitates a three dimensional visualization of the bicontinuous nanoporous structure obtained by dealloying.

The magnitude of surface stress-induced strain [2,3] in nanoporous metals is a function of the pore and ligament size. However, because of fast diffusion of Au atoms in contact with electrolytes, nanoporous gold coarsens readily, which reduces the net amplitude of surface stress-induced strain. Therefore, a method to stabilize the microstructure of nanoporous gold is necessary. A stable microstructure is also important in other fields of application where a smaller pore or ligament size is an advantage, e.g. in sensor and catalysis applications or in use of npg as reaction matrix where high surface area is necessary or in studies like mechanical properties of nanoporous metals, which depends on length scale [36,37].

The nature of the surface-stress-charge response of metal surfaces in the capacitive region of a metal-electrolyte interface can be easily understood in terms of electron theory of the clean metal surface. But in real experiment, the interaction of adsorbate from the solution with the metal surface, which largely determines the electrode behaviour in electrochemical studies, can not be avoided. Therefore, it is necessary to understand how the different electrode processes e.g. capacitive or

specific adsorption, at a given metal-electrolyte interfaces, influence the surface-stress-charge response of metal.

This work attempts to address afore mentioned issues in preparation, characterization, functional and fundamental studies in dealloying route to nanoporous noble metals and by using dealloyed structures.

Reference:

- [1] S . BAN et al., SAE Trans. *J. Mater. Manuf.* 104(1995) 700.
- [2] A.G. Evans, J.W. Hutchinson , M.F. Ashby, *Prog. Mater. Sc.* 43 (1999) 171
- [3] A. Monillet et al., *ibid.* 23 (1993) 1045.
- [4] R.W. Ertenberg, B. Andraka, Y. Takano, *Physica B* 284-288 (2000) 2022.
- [5] J. Weissmüller, R.N. Viswanath, D. Kramer, R. Würschum and H. Gleiter, *Science* 300 (2003) 312.
- [6] D. Kramer, R. N. Viswanath, J. Weissmüller, *Nano Lett.* 4 (2004) 793.
- [7] L. H. Qian, X. Q. Yan, T. Fujita, A. Inoue, and M. W. Chen, *Appl. Phys. Lett.* 90 (2007) 153120.
- [8] F. Yu, S. Ahl, A. M. Caminade, J. P. Majoral, W. Knoll, and J. Erlebacher, *Anal. Chem.* 78 (2006) 7346.
- [9] A. M. Hodge, J. Biener, L. L. Hsiung, Y. M. Wang, A. V. Hamza, J. H. Satcher, Jr., *J. Mater. Res.*, 20 (2005) 554.
- [10] Y. Ding, M.W. Chen, J. Erlebacher, *J. Am. Chem. Soc.* 126 (2004), 6876.
- [11] J.-H. Choi, K.-W. Park, I.-S. Park, K. Kim, J.-S. Lee, and Y.-Eun Sung, *J. Electrochem. Soc.*, 153 (2006) A1812.
- [12] Lockwood DJ, Pavesi L. *Silicon fundamentals for photonics applications*. In Silicon photonics: Ed: Lockwood D.J, Pavesi L, vol. 94. Berlin: Springer-Verlag; 2004. p. 1
- [13] A. G. Cullis, L. T. Canham and P. D. J. Calcott: *Appl. Phys. Rev.*, 82 (1997) 909.
- [14] M. Lipson, *Opt. Mater.*, 27 (2005) 731
- [15] Knorr, K., Huber, P. and Wallacher, D. (2007), "*Thermodynamic and structural investigations of condensates of small molecules in mesopores*", *Z. Phys. Chem.*, (in press).
- [16] Huber, P., Soprunyuk, V. P., Embs, J. P., Wagner, C., Deutsch, M. and Kumar, S., *Phys. Rev. Lett.* 94 (2005) 184504
- [17] Hofmann, T., Wallacher, D., Huber, P. and Knorr, K. *J. Low Temp. Phys.*, 140 (2005) 91
- [18] J. Banhart, *Prog. Mater. Sc.* 46 (2001) 559

-
- [19] J. Banhart, J. Baumeister, *Production Methods for Metallic Foams*, MRS Symposium Proceeding San Francisco, 521 (1998) 121
- [20] D.C. Dunand, *Adv. Engg. Mater.* 6 (2004) 369 and references therein.
- [21] H.C.Choel, J. Dong and M. Liu, *Adv. Mater.*, 15 (2003) 1610.
- [22] H. Gleiter, *Prog. Mater. Sc.* 33 (1989) 223.
- [23] H. Masuda and K. Fukuda, *Science*, 268 (1995) 1466.
- [24] K. M. Kulinowski, P. Jiang, H. Vaswani, and V. L. Colvin, *Adv. Mater.* 12 (2000) 833.
- [25] D. V. Pugh, A. Dursun and S. G. Corcoran: *J. Mater. Res.*, 18 (2003) 216.
- [26] A. J. Forty, *Nature*, 282 (1979) 597.
- [27] A. J. Forty and P. Durkin, *Philos. Mag. A*, 42 (1980) 295.
- [28] P. R. Swann: *Corrosion*, 25 (1969) 869.
- [29] T. P. Moffat, F. F. Fan and A. J. Bard, *J. Electrochem. Soc.*, 138 (1991) 3224.
- [30] G. S. Duffo, M. Giordano and J. R. Galvele, *Corros. Sci.*, 30 (1990) 1149.
- [31] J. I. Gardiazabal and J. R. Galvele: *J. Electrochem. Soc.*, 127 (1980) 255.
- [32] S. Parida, D. Kramer, C.A. Volkert, H. Roesner, J. Erlebacher, J. Weissmueller, *Phys. Rev. Lett.* 97 (2006) 035504.
- [33] D. Crowson, D. Farkas and S. G. Corcoran, unpublished work.
- [34] X. Lu, E. Bischoff, R. Spolenak and T.J. Balk, *Scripta Materialia* 56 (2007) 557.
- [35] M. E. Gurtin, *Arch. Rat. Mech. Anal.* 131 (1995) 67.
- [36] A. M. Hodge, J. R. Hayes, J. A. Caro, J. Biener, A. V. Hamza, *Adv. Engg. Mater* 8 (2006) 853.
- [37] C. A. Volkert, E. T. Lilleodden, D. Kramer and J. Weissmüller, *Appl. Phys. Lett.* 89 (2006) 061920.

Chapter 2: Background

2.1 Dealloying route to nanoporous metals and alloys

The process of dealloying is one of the phenomena related to corrosion [1], which have been exploited to synthesize nanoporous metallic structures. It involves the selective removal of one of the constituents of a binary or ternary solid solution, either by chemical or by electrochemical means, leaving behind a porous skeleton of the other element(s). One of the constituents of the starting alloy should be less noble than the other, facilitating selective removal of one of the constituents from the alloy, when subjected to an oxidizing medium or potentiostatic conditions. In electrochemical terms, the standard oxidizing potential of the less noble component should be significantly less than the more noble component. For example, in a silver-gold solid solution, silver is more reactive (or less noble) than gold, owing to its low standard oxidation potential ($E_{Au/Au^+} = +1.68V$, $E_{Ag/Ag^+} = +0.80V_{NHE}$ [2]). So that when Ag-Au alloy is dealloyed, only silver is selectively removed leaving behind the nanoporous gold. Under all experimental conditions, the potential applied for dealloying of this particular alloy (and hence to produce nanoporous gold, npg), does not exceed the equilibrium potential of the gold. Based on the difference in equilibrium electrode potentials, one can prepare npg by dealloying Ag-Au alloys, but not Au-Pt alloys.

2.1.1 Criteria of dealloying

2.1.1.1 Thermodynamics

Dealloying involves selective removal of a component from a binary solid solution AB. The free energy of each component, assuming an ideal solid solution, is given as

$$G_A = G_A^0 + RT \ln n_A \quad (2.1)$$

$$G_B = G_B^0 + RT \ln (1-n_A) \quad (2.2)$$

where n_i ($i = A$ or B) is the mole fraction of the components in the solid solution. G_i^0 is the free energy of the respective component in the standard state i.e. free state, R universal gas constant, T is the absolute temperature. For an electrochemical reaction, $G = -zFE$ and $G^0 = -zFE^0$, where E^0 is the standard electrode potential, z is the number of electrons transferred. Substituting these in to eqn. 2.1 and 2.2, one obtains

$$E_A = E_A^0 - \frac{RT}{z_A F} \ln n_A$$

$$E_B = E_B^0 - \frac{RT}{z_B F} \ln n_B$$

Difference in the potential

$$\Delta E = E_B - E_A = \Delta E^0 - \frac{RT}{z F} \ln \frac{n_B}{n_A} \quad (2.3)$$

which shows the existence of a difference in the electrochemical potential of each component in the alloy, which dependent on the difference in their standard electrode potential and the mole fraction in the solid solution.

2.1.1.2 Composition

Dealloying occurs if the concentration of the less noble component exceeds a specific limit, called the parting limit. This concept is still used in noble metal technology to separate noble from base metals. For example, an alloy of 55 at.% gold and 45 at.% silver does not dealloy, but if the atomic percent of silver in the alloy is increased to greater than 60 percent, then the alloy can undergo electrochemical dissolution in an oxidizing environment such as nitric acid or by application of a suitable potential. The concept of parting limit was introduced by Tammann [3] in 1919. Seeking an explanation for this threshold, Masing [4] calculated the probability with which a continuous filament of active (i.e. less noble) atoms would dissolve in a randomly orientated alloy in solution; the approach is presently called percolation model [7,8]. As expected, this probability depends strongly on the concentration of the active atoms.

2.1.1.3 Critical potential

The criterion of parting limit is a necessary but not the sufficient condition for dealloying to take place. As an alloy is gradually polarized positive, there is a

competition between the dissolution of the less noble element and the surface diffusion of the nobler element, depending on the magnitude of the applied potential. For bulk dealloying to take place, sufficient surface diffusion of the more noble element must occur to expose fresh alloy layers to be attacked by the electrolyte but it should not continue to the extent that the surface is passivated by accumulation of nobler element, hence impeding the dealloying. Therefore, under potentiostatic condition there exist a limiting potential below which bulk dealloying doesn't proceed. This potential is called critical potential (E_c) and characteristic of the alloy composition. Below this critical potential surface diffusion of more noble component is more predominant and with time it enriches the surface preventing a bulk dealloying. Above critical potential bulk dealloying wins over surface diffusion and evolution of porosity takes place. Thus, E_c represents a transition between surface smoothening by surface diffusion to a severe roughening leading to bulk dealloying and porosity evolution. Below E_c the current of dissolved ions from the alloy is very low, but above E_c it rises exponentially due to substantial dealloying as the structure is rapidly stripped of its less noble component. The value of E_c depends on the concentration of the more noble component (e.g. Au) and increases as its concentration increases.

2.1.2 Overview of dealloying mechanisms

A summary of the models proposed over the years, which lead to the explanation of the dealloying phenomena are discussed below. Various mechanisms have been proposed that enable porous structures formation by dealloying are; ionisation–redeposition, volume diffusion, surface diffusion and the percolation model.

Ionization–redeposition model was proposed by Brahms [5] in 1992. According to this model neither of the elements in the alloy is inert in the electrolyte, and initially they both dissolve, followed by the redeposition of the more noble element back on to the surface. But experimental works show that only one of the elements is being preferentially dissolved. In most experimental conditions, leading to nanoporosity formation, the dealloying potential is generally much below the potential required for dissolution of more noble component of the alloy. For example, in Au and Pt based systems potentials where only selective removal of the less noble component occurs, dissolution of both Au and Pt can be thermodynamically discounted, since Au and Pt has higher standard reduction potentials. From our observations, in dealloying of AgAu alloy, the crystal structure is conserved, which can be used as a proof of selective removal of Ag atoms.

In order to explain how dealloying is maintained over more than few atom layers, Pickering and Wagner [6] suggested volume diffusion, where only the less noble metal is dissolved from the alloy creating a super-saturation of vacancies at the surface. Injection into bulk of divacancies maintains the transport of the less noble components to the surface, thereby permitting propagation of the dealloying process. They described E_c as the potential corresponding to the critical concentration of divacancies. This model

is unrealistic in the context of the slow speed associated with solid state diffusion at room temperature (e.g. volume self-diffusion of Au [7] is of the order of 10^{-40} cm² s⁻¹) and the high temperatures would be required. Again, the equilibrium vacancy concentration in alloys is very low at room temperature to support a transport mechanism by vacancy injection. For example, using vacancy formation energy (E_f) of Au, as 1.57×10^{-19} J [8], its equilibrium vacancy concentration (C_{vac}) at room temperature is 10^{-17} .

Also, from the work of Keir and Pryor [9], kinetics of dealloying of three Cu alloys follow the order of Cu-Mn>Cu-Zn>Cu-Ni, but the self diffusion coefficients do not fall in the same qualitative order.

The model of surface diffusion was proposed by Forty and Rowlands [10] and Forty and Durkin [11] by studying Au–Ag and Au–Cu systems. According to this model the system is disordered by the dissolution of the less noble element and is then reordered by the surface diffusion of adatoms of the more noble element which reduces the surface energy.

Surface diffusion model was extended by incorporating percolation theory [12] in order to include the importance of the placement of atoms in a randomly packed way in the solid to account for the appearance of porous structures. Percolation deals with the degree of connectedness of components in a random system. At a threshold concentration of occupied sites, connected clusters of infinite extent is achieved which are connected through a series of specified nearest neighbors. This infinite cluster consists of a skeletal structure called the backbone, which contains the majority of the clusters with ribs branching off. It was believed that such a backbone is precursor to the nanoporous structure evolves after dealloying.

But experiments revealed that the final nanoporous structure is not based on any pre-existing structures in the alloy. The etching by the acid electrolyte creates a new network of tunnels and pores. Also, it is not sufficient for an alloy to contain a continuous filament of reactive atoms if the filament is too narrow to admit ingress of electrolyte into the resulting channel. So, dealloying must involve surface diffusion of the more noble component at the surface to open up channels for water ingress. Such dynamic processes were recently included in the numerical model developed by Erlebacher and colleagues [13,14].

2.1.3 Comparison of dealloying to other electrochemical methods

Besides dealloying, other electrochemical methods for preparing nanoporous structure are: pattern formation of semiconductors by electrochemical anodization [15], or by using anodized alumina [16], liquid crystal [17,18] and colloidal [19] templates.

The advantage of above methods is that they produce ordered array of the pores and the pore distribution can be predicted and the experimental parameters tailored to achieve these. However, porous films formed by these methods have pores on the range

of hundreds of nm where as dealloying can yield pores in sub-mesoporous the region (< 20 nm). The dealloyed porous films and the liquid crystal template porous films are potential catalytic devices. In terms of pore size the liquid crystal template is a direct competitor to the dealloyed films, besides template formations has the advantage of ordered arrays of pores. But possibility of preparing monolithic porous bodies and lower cost, gives dealloying method added advantages over liquid and colloidal crystal template approaches.

Dealloying offers an exciting route to the formation of nanoporous metals and alloys with a structure size on the scale of as low as 3 nm in diameter. It is possible to manipulate the morphology by tailoring the initial alloy composition and the dealloying potential. Even after processing, it is possible to affect the size of the pores by heat treatment.

2.2 Charge-induced strain in nanoporous metals and alloys

When a nanoporous metallic body is charged in an electrolyte, its surface electronic charge density can be varied at the metal-electrolyte interface [20]. A change in electronic structure at the surface of metal induces a change in bonding of the surface atoms; injection of negative charge increases bonding between surface atoms and reduces the bond length; bond length increases with injection of positive charge because of the reduction of bonding. This variation of bond length at the metal surface gives rise to a stress at the surface. Since whole metal lattice is coherent in a continuum model, the stress at the surface must be balanced by a pressure in the bulk. As a result, the whole body of materials expands or contracts elastically in response to the stress at the surface produced by variation of surface charge density. A schematic diagram in Fig.2.1 below depicts this mechanical equilibrium between surface and bulk in a solid.

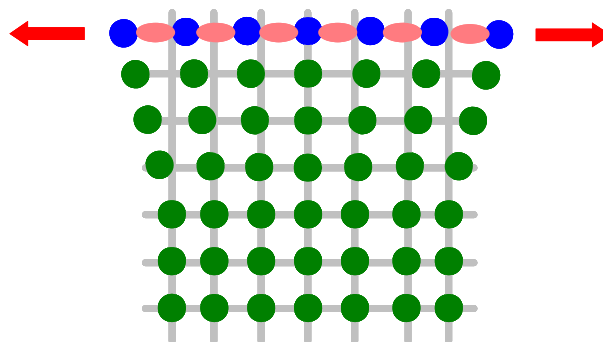


Figure 2.1 Schematic of the mechanical equilibrium between surface and bulk of a solid in response to the in-plane elastic strain at the surface. The blue and green dots represent surface and bulk atoms respectively. The arrows show the direction of the in-plane stretch. The in-plane bonds at surface favor different atomic spacing than bulk.

This mechanical equilibrium between surface and bulk is presented by [21]

$$2A\langle f \rangle_A = 3V\langle P \rangle_V \quad (2.4)$$

where f is the interface stress, which measures the forces opposing the elastic deformation of the surface and is represented as the strain derivative of the interfacial free energy, P is the pressure in the bulk, A is the total surface area and V is the total volume of the solid. Equation 2.4 relates the volumetric average of the pressure, $\langle P \rangle_V$ in the bulk of the solid to the areal average of the interface stress, $\langle f \rangle_A$ on all the surfaces irrespective of the geometry of the microstructure and serves as generalized capillary equation for solid.

The surface stress, f , is a function of the surface charge density or of the applied potential. Because of the narrow space-charge regions at metal, changes of a local property (here elastic strain), which result from the modified electronic density of states in the space-charge layer, only becomes pronounced, if the surface-to-volume ratio is extremely high [12, 15]. Because of high surface to volume ratio of nanoporous metals and alloys produced by dealloying, this surface stress induced elastic deformation is very pronounced in these nanoporous structures. This phenomenon has been demonstrated in npg prepared by dealloying [22] and nanoporous Pt compact [23], where the length change varies linearly with charge and hence with surface stress (hence the name: charge or surface stress-induced). From these observations, the total strain amplitude found in npg is 0.015% and that in nanoporous Pt compact about ten times larger than former.

The microscopic processes behind the reversible charge-induced elastic deformation of nanoporous solids are fundamentally different from the more familiar processes behind the deformation of electrostrictive materials such as ferroelectrics. In ferroelectrics, the electric field (which is only partly screened by surface charges) penetrates the material, which leads to a charge displacement throughout the bulk and consequently to a strain without stress. In contrast to this, the electric field is perfectly screened at the surface of nanoporous metals, and the strain in the bulk of the nanoporous samples arises exclusively from a long-range elastic interaction with the surface. In a reaction to change in the electric potential, there is a change in bond forces exclusively at the surface, where the excess charge is localized.

The surface stress, f , is intricately related to the surface electronic structure and bonding [24]. As explain previously, it quantifies the elastic response of the surface to the changes in the bond forces on the surface of nanoporous solids. When the surface stress becomes more tensile (more positive f), the compensating bulk stress is compressive, and the material contracts (negative strain). On an electrode surface, f varies as a function of the superficial charge density, q (or the potential, E). From its variation with the charge on electrode surface a phenomenological thermodynamics parameter, surface stress-charge coefficient ζ , can be deduces and at constant chemical potential, strain and temperature, $\zeta = \partial f / \partial q$. The surface stress-charge coefficient

essentially describes the phenomena at a metal-electrolyte interface. The sign and magnitude of ζ varies depending on the processes occurring on a metal surface and hence can be used to characterize the surface.

References

- [1] K. Sieradzki and R. C. Newman, *J. Phys. Chem. Solids*, 48 (1987) 1101.
- [2] Paul M.S. Monk, *Fundamentals of Electroanalytical Chemistry*, John Wiley & Sons 2001, pp 307.
- [3] G. Tammann, *Z. Anorg. Allg. Chem.* 107 (1919) 1.
- [4] G. Masing, *Z. Anorg. Allg. Chem.* 118 (1921) 293.
- [5] R. B. Brahm, *Trans. Am. Electrochem. Soc.*, 42 (1992) 39.
- [6] H. W. Pickering and C. Wagner, *J. Electrochem. Soc.*, 114 (1967) 698.
- [7] R.C. Jaclevic and L. Elie, *Phys. Rev. Lett.* 60 (1988) 120.
- [8] R.O. Simmons and R. W. Balluffi, *Phys. Rev.* 125 (1962) 862.
- [9] D.S. Keir and M.J. Pryor, *J. Electrochem. Soc.* 127 (1980) 2138.
- [10] A. J. Forty and G. Rowlands: *Philos. Mag. A*, 43 (1981) 171.
- [11] A. J. Forty and P. Durkin: *Philos. Mag. A*, 42 (1980) 295.
- [12] K. Sieradzki, R. R. Corderman, K. Shulka and R. C. Newman: *Philos. Mag. A*, 59 (1989) 713.
- [13] J. Erlebacher, M. J. Aziz, A. Karma, N Dimitrov & K Sieradzki, *Nature*, 410 (2001) 450.
- [14] J. Erlebacher, *J. Electrochem. Soc.*, 151 (2004) C614.
- [15] A. G. Cullis, L. T. Canham and P. D. J. Calcott, *Appl. Phys. Rev.*, 82 (1997) 909.
- [16] H. Chik and J. M. Xu, *Mater. Sci. Eng.*, 43 (2004) 103.
- [17] G. S. Attard, P. N. Bartlett, N. R. B. Coleman, J. M. Elliot, J. R. Owen and J. H. Wang, *Science*, 278 (1997) 838.
- [18] G. S. Attard, S. A. A. Leclerc, S. Maniguet, A. E. Russell, I. Nandhakumar, B. R. Gollas and P. N. Bartlett, *Micropor. Mesopor. Mater.*, 44–45 (2000) 159.
- [19] O. D. Velev, P. M. Tessier, A. M. Lenhoff and E. W. Kaler, *Nature*, 401 (1999) 548.
- [20] H. Gleiter, J. Weissmüller, O. Wollersheim, R. Würschum, *Acta Mater.* 49 (2001) 737.
- [21] J. Weissmüller, J.W. Cahn, *Acta Mater.* 45 (1997) 1899.
- [22] D. Kramer, R. N. Viswanath, J. Weissmüller, *Nano Letters* 4 (2004) 793.
- [23] J. Weissmüller, R.N. Viswanath, D. Kramer, R. Würschum and H. Gleiter, *Science* 300 (2003) 312.
- [24] W. Haiss, J.-K. Sass, *Langmuir*, 12 (1996) 4311.

Chapter 3: Materials and methods

3.1 Preparation of nanoporous gold (npg) and nanoporous AuPt alloys

In this work nanoporous samples were prepared in bulk (mm-sized) as well as thin leaf (ca.100nm) form. Bulk npg samples were dealloyed from $\text{Ag}_{75}\text{Au}_{25}$ alloy. The master alloy $\text{Ag}_{75}\text{Au}_{25}$ was prepared by arc melting Ag and Au (ChemPur, Au 99.9985%, Ag 99.99%). The ingots (~4-6g) were sealed in evacuated quartz ampoules and were homogenized by annealing at 850°C for 60h to 100h. After homogenization, ingots were rolled to form 1mm thick sheets, from which either rectangular pieces or 1mm edge length cubes were cut by a diamond wire cutting machine. Finally samples were annealed for 3h at 850°C in Ar flow for recovery and then subjected to dealloying study.

For nanoporous AuPt samples, master alloys of three compositions of $\text{Ag}_{1-x-y}\text{Au}_x\text{Pt}_y$ were used, where the Ag content in all compositions was fixed at 75 at.% and the Pt contents were varied as $y = 0.25, 2.5$ and 5 at.%. Like AgAu alloy discussed above, the ingots were prepared by arc melting Ag, Au and Pt (ChemPur, Pt 99.9985%). For proper mixing of constituents, $\text{Ag}_{1-x-y}\text{Au}_x\text{Pt}_y$ master alloys were re-melted by induction heating in a melt-spinning apparatus. For such re-melting ingots were put in quartz tubes, specially made to fit in the melt-spinning sample tube holder. Before melting, the quartz tube with the ingot were purged three times with argon gas after evacuating to 10^{-6} mbar. The heating current was gradually increased till the ingot start to turn liquid and then current was immediately brought down. After re-melting, ingots were allowed to cool under argon. The samples were cut, either as cubes or rectangular pieces, directly from the ingots and then recovered under same condition as for $\text{Ag}_{75}\text{Au}_{25}$ alloy samples.

Besides the bulk $\text{Ag}_{75}\text{Au}_{25}$ alloy samples discussed above, a form a very thin (ca. 120nm thick) samples were also used in dealloying study and characterization study, which are obtained from commercially available gold leaf [1]. Gold leaves have a long history of application in gild art and decorative surfaces. These samples are prepared by multiple folding and hammering of gold or gold-silver sheets, until, a delicate, less-than-paper-thin sheet or “leaf” of gold is formed. Gold leaf was obtained from the commercially available white gold leaf (120 nm thick) of two qualities: 6 carat (Wasner Blattgold GmbH, Schwabach, Germany), and 11 carat ("Monarch", Sepp Leaf Products, New York). Energy-dispersive x-ray fluorescence (EDX) data indicate the compositions $\text{Ag}_{80}\text{Au}_{20}$ and $\text{Ag}_{67}\text{Au}_{33}$ for the 6 and 11 carat samples, respectively. Advantage of such sample is that they can be used directly for electron microscopy without any further sample preparation.

For all compositions, electrochemical dealloying was carried out in one molar perchloric acid (1M HClO_4) at ambient temperature under potential control using a potentiostat (PGSTAT 100 EcoChemie, Autolab), Ag/AgCl reference and coiled-Ag wire counter electrodes (CE). Dealloying was interrupted when the current fell to $10\mu\text{A}$ at which time nearly all Ag was removed from the alloy; for bulk $\text{Ag}_{1-x}\text{Au}_x$ this took about 6-10 hours, depending the potential applied and sample size, and for thin gold leaf samples complete dealloying took about 1-2 minutes.

The Ag/AgCl pseudo-reference electrode was prepared by oxidizing a Ag wire at 1V for about 40s in 1M HCl. 1M HClO_4 was prepared from 70% perchloric acid of Suprapur[®] grade from Merck. For proper cleaning, all the glass wares and sample cells were cleaned in H_2SO_4 and H_2O_2 (7:1 vol. %) mixture and soaked in ultrapure water (18M Ω) for overnight.

The experimental sets up for insitu strain measurements during dealloying were different for mm-sized bulk sample and thin gold leaf samples and are explained in the following sections.

3.2 Insitu strain measurements during dealloying

To study the effect of dealloying on sample dimension, dimension changes of the samples were followed insitu during dealloying. Two different approaches were followed for bulk and thin leaf samples and are discussed as below.

3.2.1 For bulk $\text{Ag}_{75}\text{Au}_{25}$ and $\text{Ag}_{1-x-y}\text{Au}_x\text{Pt}_y$ alloys

In the case of bulk samples, in-situ measurement of strain was performed using miniaturized electrochemical cells (electrolyte volume about 5-10ml) mounted in a commercial dilatometer such as Netzsch 402C with horizontal push rod and Linseis with vertical push rod, with sensitivity ca.5nm. The variation in sample length produced during dealloying is transmitted to an inductive displacement sensor via a vertical or horizontal pushrod loaded by a fixed contact pressure of 20cN. Cube samples of 1mm

edge length, used for dealloying study, were mounted between support and pushrod. For 1mm^2 area of the samples used and for the contact pressure of 20cN , the stress exerted by the dilatometer probe is about 0.2 MPa , insignificantly small as compared to the yield strength of nanoporous gold ($\sim 100\text{ MPa}$) [2]. A schematic diagram of the experimental set up for insitu strain measurement during dealloying in a dilatometer is shown in figure 3.1.

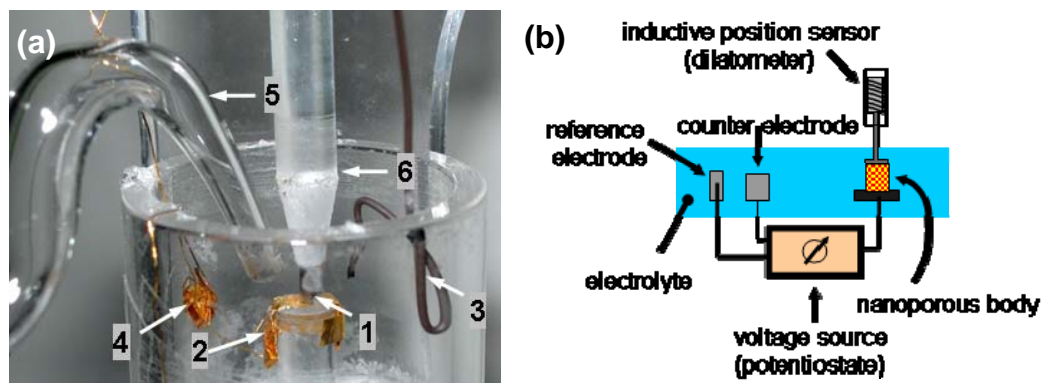


Figure 3.1 a) A picture of dilatometer sample space modified for insitu dealloying of bulk samples, showing, 1: alloy sample, 2: a gold foil for electrical contact to the sample, 3: reference electrode, 4: CE used for the strain measurements after dealloying. This is not electrically connected during dealloying, 5: an external quartz tube in which the Ag-wire CE used for dealloying, was placed. This tube along with the Ag-wire CE was removed after dealloying, 6: dilatometer push rod; b) A schematic arrangements of the set up as in (a).

3.2.2 For gold leaf samples

In case of leaf samples, dealloying condition is same as bulk samples described above. Leaf samples were kept floating on the electrolyte and electrical contact was made by touching the sample with a thin gold wire. A spiral or a ring shaped Ag wire CE was used with the main objective of using a CE with larger surface area, but it should be mentioned that the result was never influenced by if the CE is a ring or a spiral. The CE was placed below the sample and the cell was completed by attaching an Ag/AgCl reference electrode. With a pre-fitted digital camera, pictures of the alloy leaf were taken before and after dealloying. From the comparison of the edge widths before and after dealloying, the reduction of dimension after dealloying was calculated. Minimum length change measured from the picture was 1mm . A schematic arrangement for dealloying of leaf samples is shown in figure 3.2.

3.3 Reversible strain measurements in nanoporous Au and AuPt alloys

The experimental set up used for reversible strain measurements in nanoporous metals and alloys was the same as that used for studying strain during dealloying of bulk samples (see Sec.3.2.1). Only difference is, the Ag wire CE used for dealloying was separated from the main cell containing the sample by placing it in a quartz tube containing the same solution, with the tube opening close to the sample.

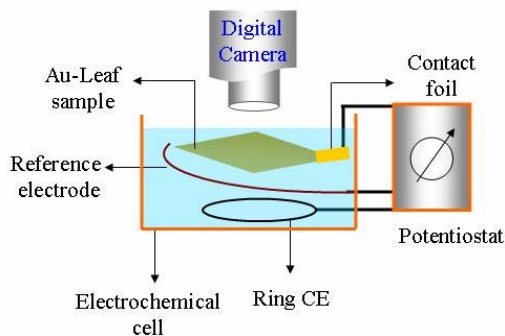


Figure 3.2 Schematic arrangements for dealloying of thin leaf samples.

Such an arrangement was helpful in reducing the silver contamination in the main cell after the dealloying. The quartz tube with the Ag wire CE was detached from the cell containing the sample, after dealloying. Another piece of pre-dealloyed npg or nanoporous AuPt, placed in the same cell as sample, serve as the CE for subsequent reversible strain measurements. Repeated cleaning procedures were followed to remove traces of Ag left over from dealloying. This involves rinsing the main cell several times with the solution which is to be used next for the measurements. While changing one solution to another, the cell was first cleaned by ultrapure water (18M Ω) and then rinsed with new solution. Sometimes, fast potential cycling was carried out during rinsing with a solution, with an objective to properly wet the small pores in nanoporous sample with new solution.

As above the potential was controlled by a potentiostat. All potentials are referred to Ag/AgCl reference electrode. Several successive scans were taken by varying potential at a fixed scan rates and simultaneously the length change of the sample was followed by the dilatometer. The length variation signal from dilatometer was acquired instantaneously through the potentiostat equipped with an analogue digital converter module. The charge, Q , transferred to the sample during potential scans was determined by integration of the current transient using the potentiostat's "current integration" mode.

3.4 Transmission electron microscopy of npg

Transmission electron microscopy (TEM) studies on npg were done with a Philips FEI Tecnai F20ST field-emission gun (FEG)-TEM operated at 200 kV. Nanoporous gold was prepared by dealloying as-received 6 carat white gold leaf, under the same condition as explained in Sec.3.1. The npg obtain this way is 100 nm thick and does not need further sample preparation for TEM investigation [3].

3.5 Z-contrast tomography

For proper topographical and microstructural studies, a three dimensional TEM (3D-TEM) analysis was carried out on npg. High angle annular dark-field scanning transmission electron microscopy (HAADF-STEM) imaging was used for this 3D-tomography. HAADF-STEM imaging uses Rutherford scattering [4,5] between electron and the atomic nuclei in the specimen. The intensity scales with the atomic number ($Z^{-1.7}$) (hence the name Z-contrast tomography) and with the projected sample thickness [4]. HAADF-STEM imaging is well-suited for electron tomography of crystalline materials [4,6] since the contrast does not suffer from diffraction effects except when the observation area is imaged along a major zone axis. Since major zone axes are rarely encountered during the acquisition of image series, the overall effect on 3-D reconstructions is small [4]. However, limits to the resolution of the reconstructed volume are imposed by the restricted tilt range (missing wedge problem), which results from the pole piece/sample holder geometry.

The different steps followed to carry out Z-contrast tomography of npg are explained as below.

3.5.1 Acquisition of tilt series of 2-D projections

This is done by tilting the sample in steps in a wide angular interval. A series of 2-D projections, thus obtained, are called the image or data stack. In this experiment, HAADF-STEM tomography was carried out in a TEM (same model as in Sec.3.4) fitted with a Fischione HAADF detector (model FP-5360/20). Single-axis tilt series were acquired automatically using the Xplore3D 2.0 Tomography suite operated in the HAADF-STEM mode with a nominal spot size of 1 nm. A camera length of 70 mm (corresponding to a minimum scattering angle of 50 mrad) was used for the signal collection in order to minimise diffraction effects. Images were scanned with 1024×1024 pixels using a frame time of 12.5s. 73 electron micrographs have been collected over a tilt range of $\pm 66^\circ$ in 1.8° steps. Re-centring and refocusing were done automatically.

3.5.2 Reconstruction of 3D image from the data stack

Reconstruction of 3d image from the data stack involves alignment of data stack and 3D reconstruction by iterative back projection. The alignment of the individual stacks and the reconstruction of the acquired tilt series was done off-line using FEI's software package Inspect 3D version 2.1. The tilt series alignment was made by iterative cross-correlations to sub-pixel accuracy.

The principle of reconstruction is the following. The projection of a 3D object is the central portion of the Fourier Transform (FT) of that object. Thus the tilt series provide many different central sections of FT of the sample; thus filling the 3D Fourier space. By inverse FT of the obtained Fourier space a 3D picture of the original object is

obtained. The aligned tilt series was, thus, reconstructed using the iterative back-projection process SIRT [7] which is implemented in the Inspect 3D code. 25 iterations were performed for the SIRT reconstruction. Each three-dimensional pixel ('voxel') of the reconstruction represents a cube with an edge-length of 0.73 nm. The software package Amira 3.1 has been used for the visualization of the reconstructed structures.

3.6 Stereological analysis of tomography of npg

The reconstruction was binarized for stereological analysis and then cropped in all spatial directions (to 340 nm × 300 nm × 70 nm) in order to remove the macroscopic sample surfaces. This was done to avoid artefacts at the borders of the reconstruction, and to ensure that the volume used for analysis is representative of the bulk sample structure. The analysis was performed using the program MAVI [8]. MAVI affords a characterization of 3-D structures by analysis of their representations as binary and spatially discrete images, using the algorithms described in Ref. [9].

3.7 X-ray diffraction and texture measurement

X-ray diffraction of npg prepared from gold leaf was carried out in both transmission and reflection geometry. In reflection mode Bragg-Brentano geometry was used in a Philips X'Pert θ - θ diffractometer with Ni-filtered Cu-K $_{\alpha}$ radiation and a position-sensitive solid state detector. X-ray diffraction in transmission geometry was carried out with a Stoe powder diffractometer with Cu-K $_{\alpha 1}$ radiation and a gas-filled position-sensitive detector. Both machines use detectors with no secondary beam monochromators. For X-ray diffraction in reflection mode, thin gold leaf samples were supported on a Si single crystal and for X-ray diffraction in transmission mode free-standing gold leaf samples were used.

Texture in gold leaf samples before and after dealloying was measured in X-ray texture diffractometer from PHILIPS X'Pert MRD, equipped with horizontal Goniometer, open Eulerian Cradle and a proportional counter detector. On the primary side the parallel divergent beam from a polycapillary x-ray lens has a resolution of 0.3° with high intensity gain reducing the defocusing effect. On the secondary side the reflected beam passes through a graphite monochromator which reduces the background and suppresses Bremsstrahlung and K $_{\beta}$ radiation. The results and pole figures were generated from the data using Philips X'Pert Software.

In the texture analysis the orientation distribution of a certain crystallographic plane is determined. Prior to texture measurement, a normal x-ray diffraction pattern of the sample was taken in Bragg-Brentano geometry. Then the variation of intensity of a given hkl reflection was measured for different spatial orientation of the sample, keeping the Bragg angle fixed at that desired reflection. This was done by rotating the sample about the normal to its surface (ϕ axis) and tilting at different ψ angles with respect to the incident beam, in an Euler circle.

For texture analysis before and after dealloying, gold leaf samples were supported on a Si single crystal, as in case of X-ray diffraction in reflection mode.

3.8 Data processing

Using surface stress induced strain phenomenon as introduced in previous chapter in Sec. 2.2, the surface stress-charge coefficient, ζ can be measured in a dilatometer, from the variation of length change (δl) of the sample in response to the superficial charge (Q) variation on a metal surface.

The volumetric mean of the pressure, P , in the bulk of the material is related to the area average surface stress via equation 2.4 (Sec.2.2).

Where A and V denote the total surface area and the total volume, respectively, and the brackets denote the respective averages. Lets assume a linear relation between f and charge density (per unit area), q , $\delta f = \zeta \delta q$. For a linear elastic response, $\delta P = -K \delta V_S / V_S$, where K is the bulk modulus and V_S the total volume of the solid. The variation of net charge is given as, $\delta Q = A \langle \delta q \rangle_A$, where $\langle \delta q \rangle_A$ is the area average of the charge density, i.e. q per unit area, A . By insertion of these relations into eqn.2.4 one obtains

$$-3 K \delta V_S = 2 \zeta \delta Q \quad (3.1)$$

If all ligaments in the npg would strain isotropically and uniformly, then the macroscopic length change as measured in the dilatometer, δl , would relates to the volume change of the solid via $3 \delta l / l = \delta V_S / V_S$. This relation has been confirmed by in-situ x-ray experiments during electrochemical cycling of porous Pt prepared by consolidation of nanopowder [10].

Substituting in Eq. (3), $V_S = m / \rho$ where m and ρ denote the sample mass and the density of the solid phase, respectively,

$$\zeta = -\frac{9 K m \delta l}{2 \rho l \delta Q} \quad (3.2)$$

where ζ is related to the measurable quantities like the macroscopic strain $\delta l / l$, the transferred charge δQ and the sample mass m . It is important to note that the evaluation of ζ from eqn.3.2 does not require the knowledge of specific surface of the sample. Thus, for a given type of surface (i.e. given value of ζ), the relation between length change and total charge is independent of the size and geometry of the microstructure.

References

- [1] Y. Ding, Y.-J. Kim, J. Erlebacher, *Adv. Mater.* 16 (2004) 1897
- [2] J. Biener, A.M. Hodge, A.V. Hamza, *Appl. Phys. Lett.* 87, 121908 (2005).
- [3] S. Parida, D. Kramer, C. A. Volkert, H. Rösner, J. Erlebacher and J. Weissmüller, *Phys. Rev. Lett.* 97 (2006) 035504
- [4] C. Kübel, A. Voigt, R. Schoenmakers, M. Otten, D. Su, T-C. Lee, A. Carlsson, and J. Bradley, *Microsc. Microanal.* 11 (2005) 378.
- [5] P.A. Midgley and M. Weyland, *Ultramicroscopy*, 96 (2003) 413.
- [6] M. Weyland, T.J.V. Yates, R.E. Dunin-Borkowski, L. Laffont, and P.A. Midgley, *Scripta mater.* 55 (2006) 29.
- [7] P. Gilbert, *J. Theor. Biol.* 36 (1972) 105.
- [8] http://www.itwm.fhg.de/mab/projects/MAVI/index_de.php
- [9] J. Ohser and F. Mücklich, *Statistical Analysis of Microstructures in Materials Science*, John Wiley & Sons, Chichester 2000, Ch. 3-4.
- [10] J. Weissmüller, R.N. Viswanath, D. Kramer, R. Würschum and H. Gleiter, *Science* 300 (2003) 312

Chapter 4: Characterization of the microstructure

4.1 Introduction

A detailed characterization of microstructural and topological properties of npg include quantitative information on the porous structures, such as specific surface area, distributions of pore and ligament sizes, network or ligament connectivity and structural anisotropy. Such detail information on the porous microstructure was not revealed from conventional electron microscopy studies carried out previously [1,2]. Therefore, a study of the npg microstructure using 3-D electron tomography in a transmission electron microscope (TEM) is presented, which addresses the aforesaid issues, and highlights inadequacies in a conventional electron microscopy study of a porous microstructure. The observations reveal a single crystalline microstructure in contrast to a nanocrystalline microstructure reported previously [3].

Also discussed in the chapter, is the effect of dealloying on the grain size of the original alloy as probed by X-ray diffraction and texture analysis carried before and after dealloying.

4.2 X-ray diffraction of npg

X-ray diffraction of npg dealloyed from 6 carat Au leaf in 1M HClO₄ at 800mV was carried out both in reflection and transmission geometry and is presented in figure 4.1. The diffraction patterns are consistent with the starting material being single-phase Ag-Au alloy and the npg being crystalline Au. Lattice parameter (a) refinements yield a = 408.0(1) and 406.9(1) pm for master alloy (original gold leaf) and porous Au respectively. For the as-received sample (dotted patterns, in Fig.4.1 a & b) the ratio of

$\langle 111 \rangle$ reflection intensity over that of $\langle 200 \rangle$ deviates significantly from the value of 2:1, which would be the ratio for an untextured fcc metals. This indicates a $\langle 200 \rangle$ texture. This is apparent in both the reflection and transmission geometry data. Presence of texture is readily understood as a result of the severe mechanical deformation produced during preparation of gold leaf as discussed in chapter 2. By comparing the diffraction data for the porous gold samples to those of the as received gold leaf it is seen that the intensity ratio is maintained. This indicates that the texture does not change during dealloying.

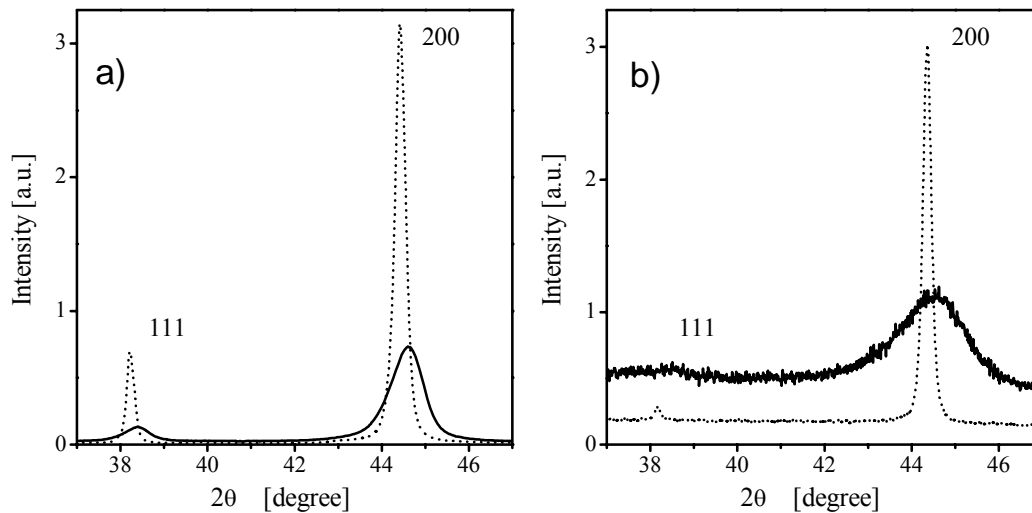


Figure 4.1: X-ray diffraction patterns (Cu-K α) of Ag-Au leaf (Wasner, 6 carat) before (dotted) and after (continuous) dealloying in 1M HClO₄ at 800mV, in (a) reflection Bragg Brentano geometry and in (b) transmission geometry. The peak intensity ratio is conserved, indicating that the 200-texture is retained during dealloying.

The observation of retention of texture during dealloying is also apparent from texture analysis of 6 carat gold leaf before and after dealloying. Figure 4.2a and b shows, 200-pole figure of the 6 carat gold leaf sample, before and after dealloying, respectively. In both the pole figures, the intensity maximum occurs in the centre, indicating the cube plane parallel to the leaf plane and a strong 200-texture. The 111-pole figures (Fig. 4.2c and d) shows the intensity is spread over the whole ϕ range without a clear maximum, which indicates no strong orientation preference in this crystallographic direction.

The retention of strong 100-texture before and after dealloying indicates that the crystal orientation remains unchanged during dealloying. The implication of this observation on the dealloying mechanism will be discussed in more details in the next chapter (Chapter 5).

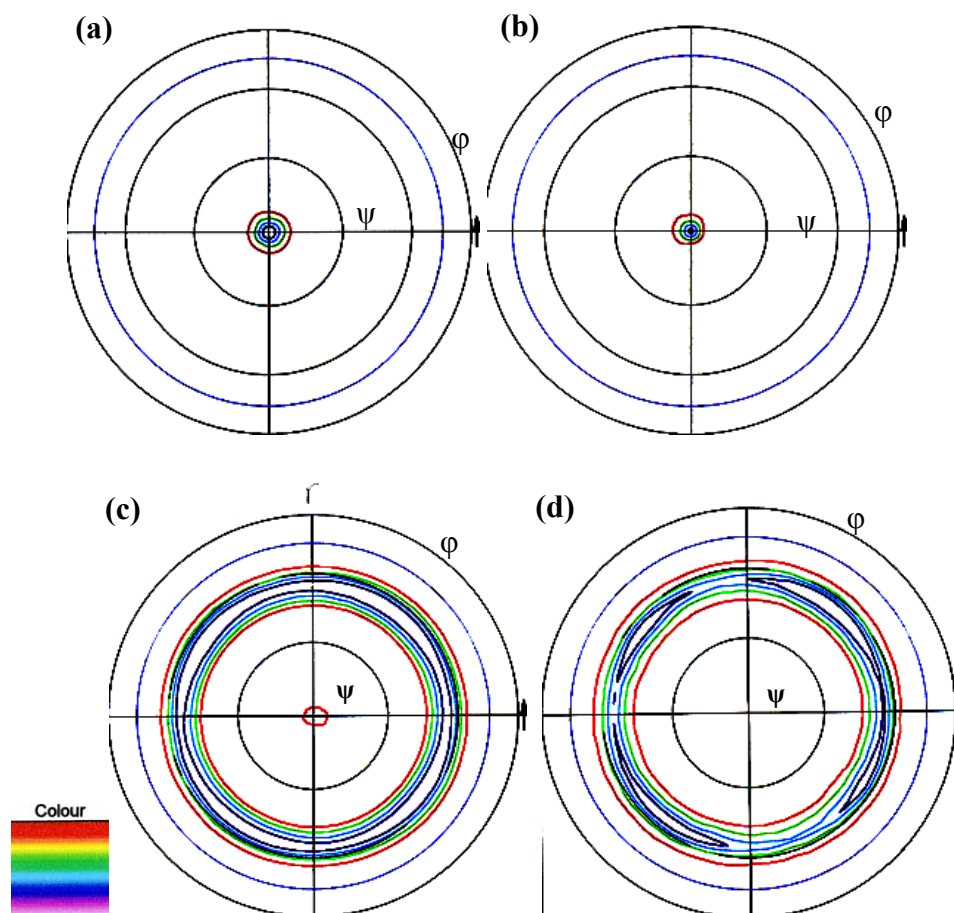


Figure 4.2: X-ray texture analysis of 6 carat Au-leaf ($\text{Ag}_{80}\text{Au}_{20}$), using Cu- $K\alpha$ radiation; (200) pole figure **a**) before and **b**) after dealloying; (111) pole figure **c**) before and **d**) after dealloying. Color codes represent the intensity in the order red (lowest), blue (medium) and magenta (highest). Φ is varied from 0° to 360° at 90° intervals and ψ is varied from 0° to 90° at 30° intervals. Pole figures indicate the 100-texture is retained during dealloying.

4.3 TEM micrographs of npg

Figure 4.3 shows the typical bright-field TEM micrograph of npg obtained by dealloying of 6 carat gold leaf in 1M HClO_4 at 600 mV (vs. Ag/AgCl). The micrograph illustrates the typical microstructure of npg, which is composed of nanometer size ligaments and pores. Darker regions in the picture represent a higher density of gold ligaments due to the overlap in the 2-D projection.

A selected area electron diffraction (SAED) pattern (the aperture corresponds to a circular area of about 800 nm in diameter) from the same volume as shown in figure 4.3 (inset) reveals a preferred $\langle 100 \rangle$ out-of-plane orientation. This is consistent with the findings of x-ray diffraction and texture analysis, discussed in previous section. Presence of discrete diffraction maxima in the SAED pattern indicates that the observation area is essentially a coherent crystalline region. However, the azimuthal width and granularity of the peaks indicate significant spread in crystal orientation in

the sampled volume, indicating the presence of strain inhomogeneities and/or lattice defects, in agreement with the findings in Ref [4] and will be covered in details in the next chapter, in relation to the effect of dealloying on sample dimension.

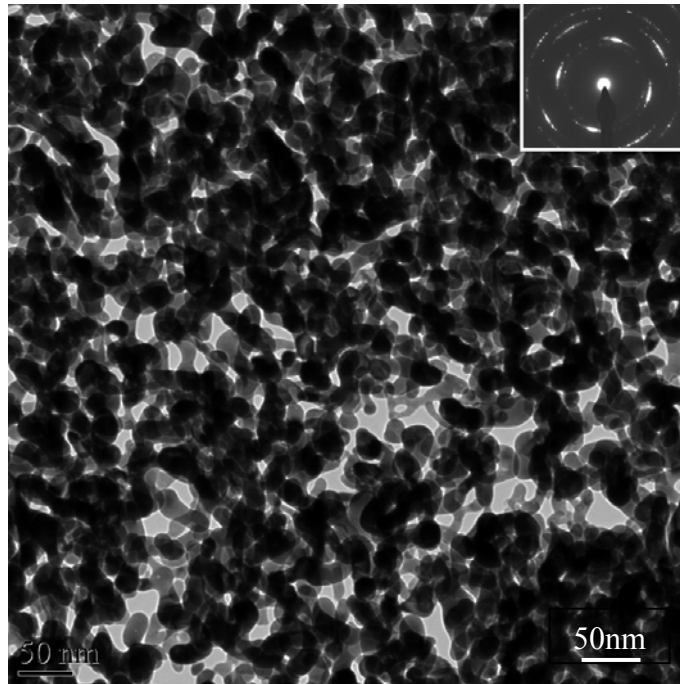


Figure 4.3. A bright-field TEM micrograph of npg, obtained by dealloying 6 carat Au-leaf at 600mV, showing a fully connected network structure. The diffraction pattern (SAED) (inset in Fig. 1a) indicates a preferred $\langle 100 \rangle$ out-of-plane orientation with considerable mosaic spread.

A detail view of individual gold ligaments in the above sample is shown in figure 4.4. A noteworthy observation is the presence of numerous spherical voids with diameters ranging from 1 to 5 nm, within the ligaments, indicated by arrows in figure 4.4. As discussed latter, these voids are also observed in the 3-D reconstruction of the sample discussed in latter section.

The micrographs presented above in figure 4.3 & 4.4, give a 2-D projection of inherently 3-D sample and only reveal information about the average density along the beam direction. When projected in 2-D, structural features in a 3-D sample like npg, are overlapped and hence the microstructural details like pore structure and shape, extent of ligament inter-connectivity, are lost. For example, from figures 4.3 and 4.4, only information on the structure of the pores can be deduced parallel to the plane of projection. Consequently, resolution in third dimension is only marginally better than the thickness of the sample. Therefore, it is necessary to obtain 3-D micrographs of the sample to get a complete picture of the inherent microstructure to determine the exact material properties.

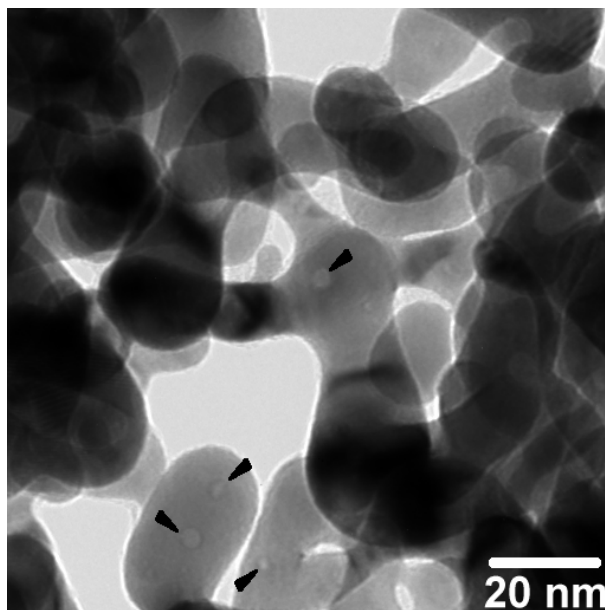


Figure 4.4. Bright-Field micrograph of sample dealloyed at lower E_D (600mV) revealing details of individual gold ligaments. Presence of encased voids in ligaments is identified by arrow heads.

4.4 3-D reconstruction of npg

Two different views of the 3-D density distribution of a 350 nm x 300 nm x 200 nm volume of nanoporous gold leaf reconstructed from HAADF-STEM tomography are displayed in figures 4.5a & b. Obvious features in figure 4.5(a) are the high connectivity and the large variation in ligament and pore size. From the cross-sectional view of the reconstruction, as in figure 4.5(b), the sample surfaces are found to be planar and at this location the leaf is around 90 nm thick. The thickness of the leaf varied from position to position and the thinnest regions were chosen for the analysis.

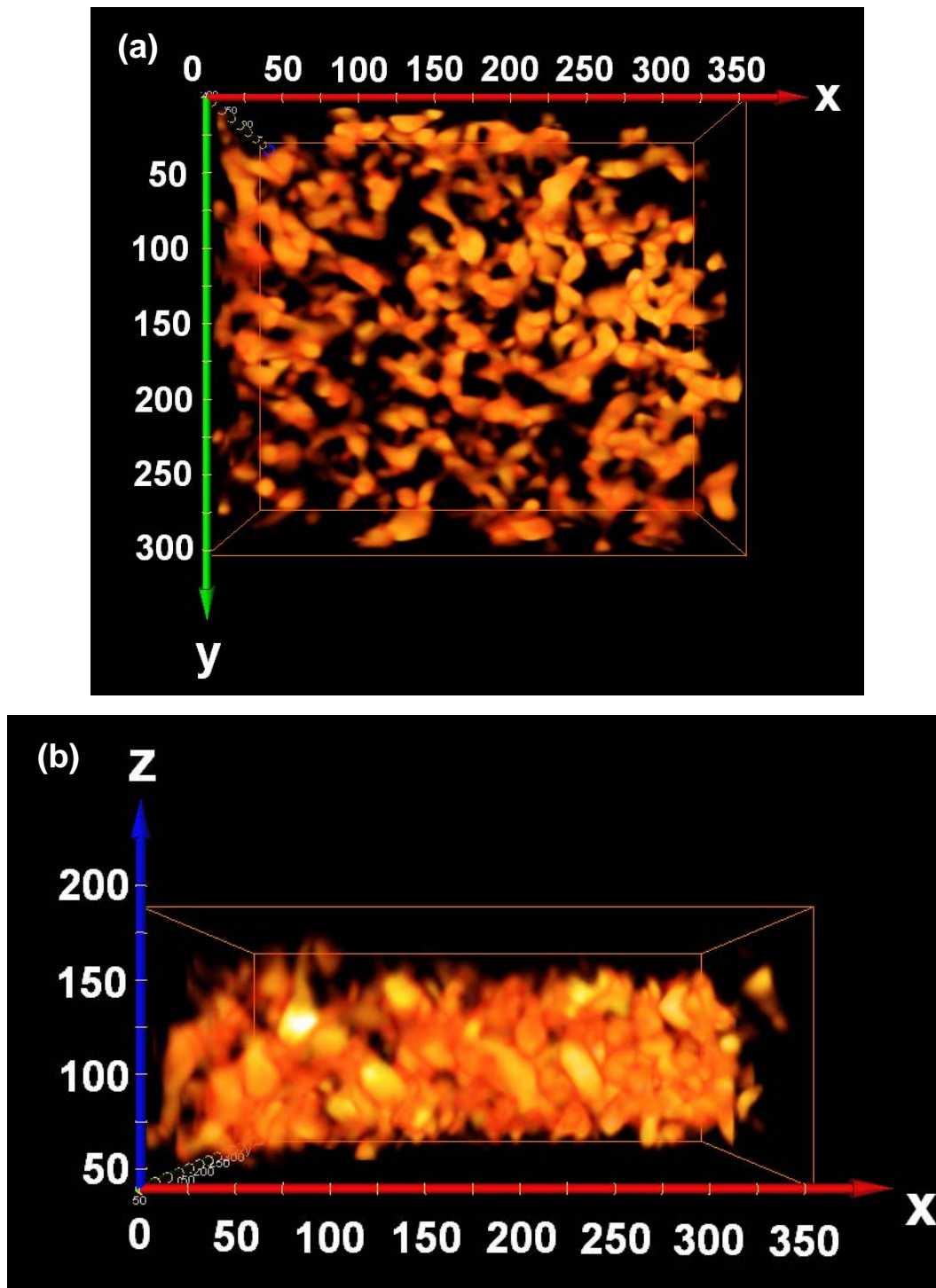


Figure 4.5. Rendered volume of the reconstruction showing the 3-D structure of the dealloyed gold leaf sample. a) X-Y (in-plane) view. b) X-Z view of the inspected volume. Axis labels give position in nm.

In figure 4.6 individual slices through the reconstructed volume is presented, which allows more detail analyses of the porous structure. The slices have a thickness of a single voxel, so that the brightness in the images is linearly related to the reconstructed density. Since the actual density of the gold ligaments may certainly be identified with that of crystalline gold, the variations in brightness shown in the images

must reflect smearing of the actual structure by the reconstruction process. Despite this blurring – which is at a length scale of around 1 nm – many aspects of the 3-D structure are revealed.

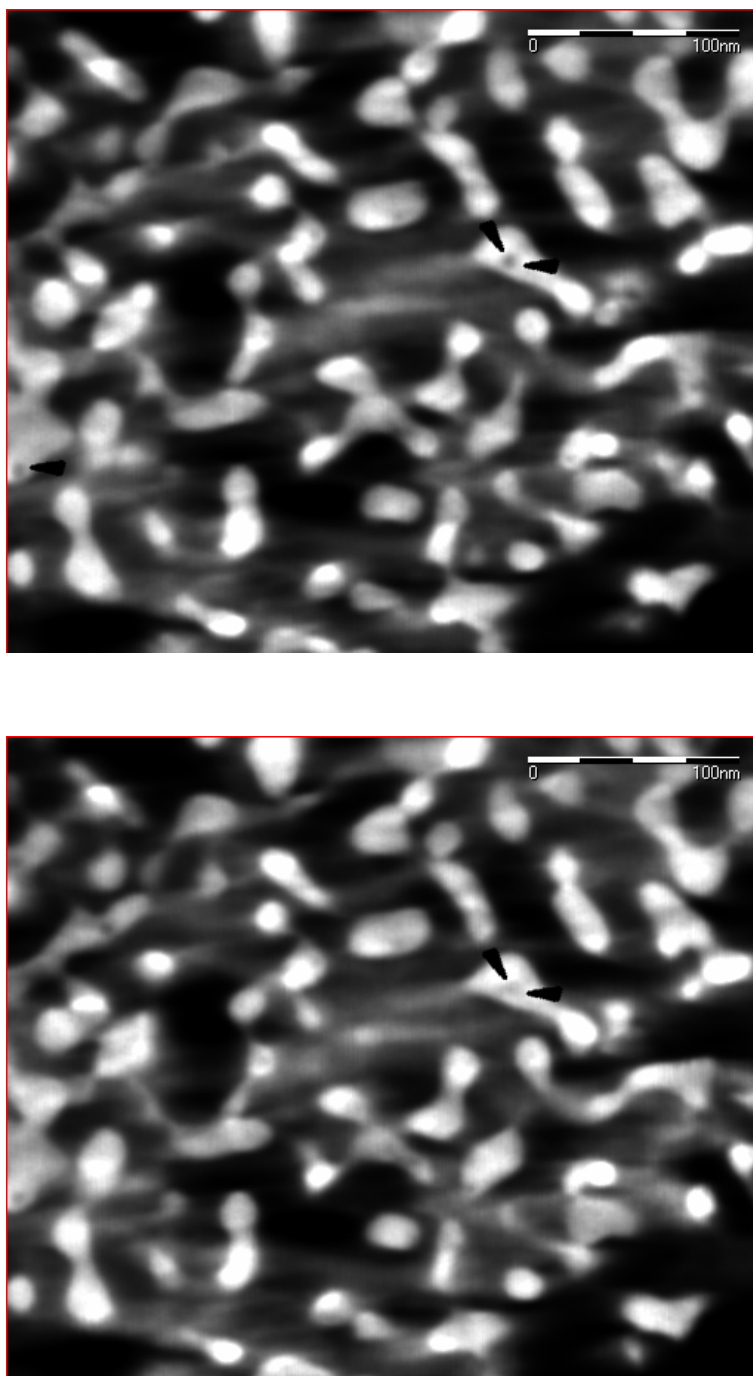


Figure 4.6 Two neighbouring X-Y slices through the reconstructed nanoporous gold volume. The brightness scales with the reconstructed local density. Arrows indicate voids inside the ligaments.

Enclosed voids within ligaments are abundant in the slice through the reconstruction shown in Fig. 4.6 (indicated by arrows). These features are also visible

in the bright field micrographs presented in figure 4.4. As compared to the size of the interconnected pores, the voids in the ligament are much smaller, of the order of 1-5 nm. Since the encased pores are also apparent in the non-reconstructed images, they cannot be a reconstruction artefact.

For better visualization of the microstructure, the 3-D reconstruction was binarized. Surface renderings of the binarized structure are shown figure 4.7. The threshold value for binarization was determined by careful comparison between slices of the binarized structure, the reconstructed densities (from Fig. 4.6) and by making sure that there be no ‘free-floating’ gold segments.

From figure 4.7(a) it is clear that the microstructure of npg is quite non-uniform: the diameter of the ligaments varies from less than 5 nm for the thinnest bridges to more than 30 nm for the thickest bulges, which occur mainly in the interior of the sample. The wide range in pore sizes distribution is another aspect of structural diversity. A detailed view of reconstructed volume in Fig 4.7b shows existence of small and quite complex pores and almost circular ligament rings of various sizes.

The images (Fig. 4.7 **a** and **b**) do not show features typically associated with that of a porous foam, although part of the relevant literature [5,6,7] refers to nanoporous metals made by dealloying as ‘foams’. Most notably, neither one cannot naturally identify distinct cells in the pore phase, nor do the ligaments resemble remnants of cell walls or triple lines. Rather, the configurations illustrate a complex topology. As shown in Fig. 4.7c one can see regions where three, four, or even five ligaments meet each other. However, the junctions do not typically appear as clearly formed nodes, and in many instances it is not obvious to discriminate between, for instance, two closely spaced bifurcations and a single, four-coordinated node. Thus, without first skeletonizing the structure, there is no obvious way to estimate the characteristic number of ligaments connected in a node.

‘Dead end’ ligaments, that is, unconnected protrusions which are at least as long as they are wide, are found mostly at the surface of the sample. The small number of ‘dead ends’ within the bulk of the structure is remarkable for the following reason: the synthesis of the porous structure involves considerable coarsening [5] resulting in a reduction of surface area, increase of the characteristic structure size, and decrease of the number of ligaments per volume. The fundamental process would seem to be curvature-driven diffusion, with redistribution of matter away from the thinnest ligaments and towards the thickest nodes. This is similar to Plateau-Rayleigh instability [8]: cylinders with surface tension are unstable when their aspect ratio (length over diameter) exceeds the value of π . Here, this results in pinch-off of thin ligaments, and hence in the formation of ‘dead ends’. Apparently, these ‘dead ends’ vanish quickly (which would be in keeping with their small size and large mean curvature), so that few of them are observed at any given time.

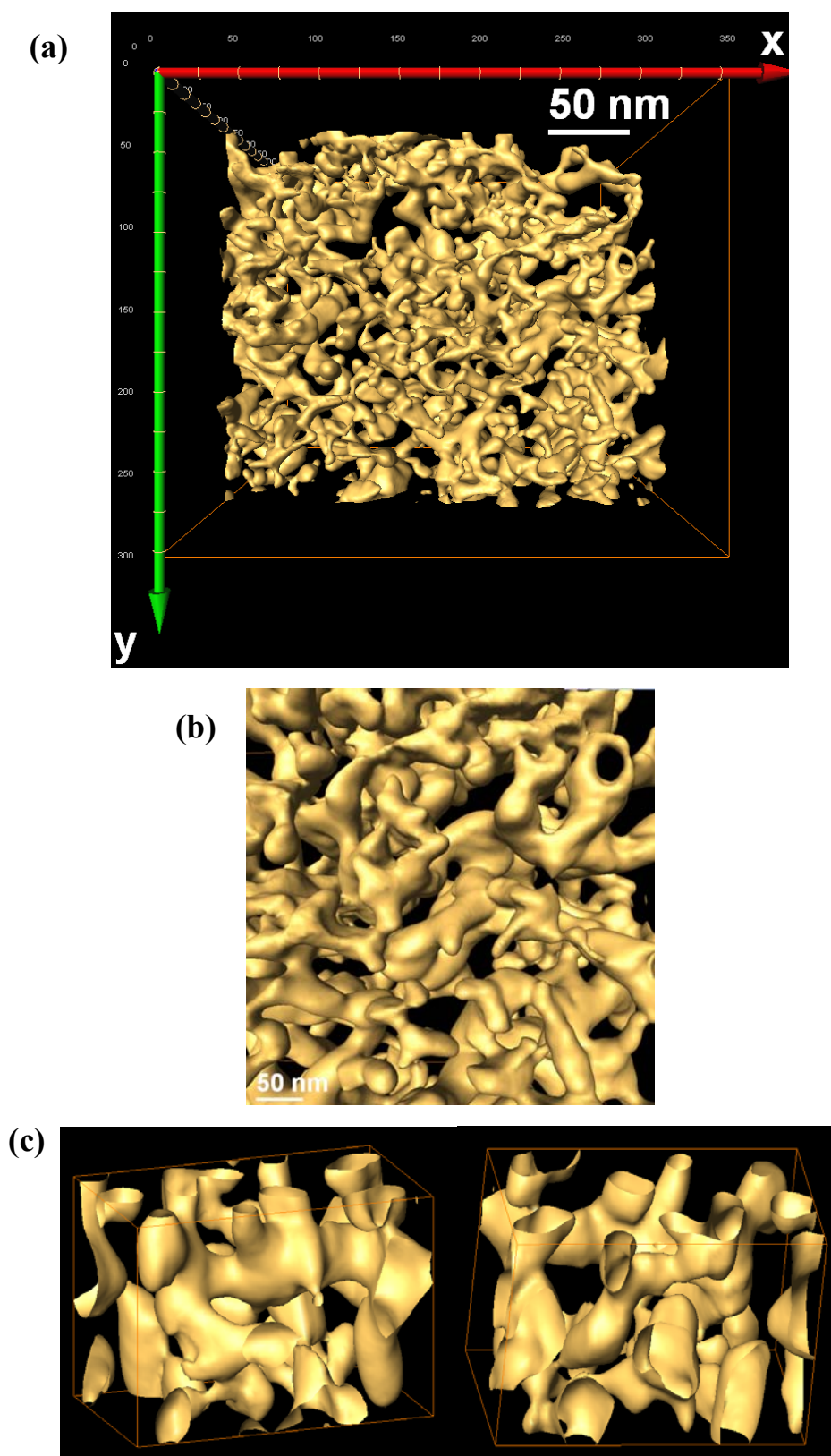


Figure 4.7 a) Surface rendering of the solid phase in the binarized, reconstructed image of nanoporous gold leaf. The macroscopic sample geometry is a sheet, and the x- and y-coordinates in the figure are in-plane. b) Detail of (a). View into the bulk with one of the samples surfaces in the foreground. c) Detail of (a). A volume element cut from the bulk, viewed from different directions. Note the complex topology of the ligaments. Sheet normal is along the vertical edges of the bounding boxes. Horizontal edges are 150 nm long.

4.5 Stereological analysis

Stereological analysis of a volume cropped from the binarized structure was performed using MAVI [9]. Since the stereological parameters depend significantly on the binarization threshold value, parameter intervals are quoted for the maximum allowable range of threshold values which yields a structure without ‘free-floating’ segments and in qualitative agreement with the structures shown in Figures 4.6 a and b. Results of stereological analysis are discussed as below.

4.5.1 Porosity

The porosity obtained from the stereological analysis of the binarized reconstructed sample is 76 ± 1 vol.-%. An independent estimate for this parameter can be obtained as follows: Since the residual Ag fraction in the nanoporous gold sample is 4 at.-%, dealloying removes 79.2 % of the all atoms from the crystal lattice of the $\text{Ag}_{80}\text{Au}_{20}$ master alloy. This would lead to a porosity of 79.2 vol.-% in the idealized case of a constant sample size. Using the procedures described in Ref. [5], it was found a macroscopic volume reduction of about 4%, which decreases the pore volume while leaving the volume of solid phase invariant. Thus, the final porosity is estimated to be 76 vol.-%, which is in good agreement with the results of the stereological

4.5.2 Ligament- and pore size distributions

First estimates of characteristic pore- and ligament sizes are obtained from the mean chord lengths of their respective phases in the binarized structure. The values are 55 and 17 nm for pores and ligaments, respectively. For a more detailed picture, the pore and ligament sizes were quantified using granulometry [12,10], where the pore or ligament space was completely filled by overlapping spheres of different sizes, and each voxel in the phase was assigned to the largest sphere in which it was contained. The resultant distributions of sphere radii for the pores and ligaments, shown in Figures 4.8 (a) and (b) respectively, can be interpreted as a volume weighted local feature size. The granulometry distributions were approximated by Gaussians and the peak positions at 28 ± 8 and 16 ± 5 nm corresponds, respectively, to pores and ligaments. These values for pore and ligaments can be taken as a measure of the mean pore and ligament radius. The interval is, then, the variance of the Gaussian fit. Simple structural models for porous materials [11] can be used to relate these mean feature sizes to the volume fraction $q \approx (\text{ligament radius/pore radius})^2 = 0.29$. The reasonable agreement of the predictions of the simple structural models with the volume fraction of the reconstruction ($q = 0.24$), provides support for using these models to interpret general properties of nanoporous gold, such as mechanical behaviour [12, 8].

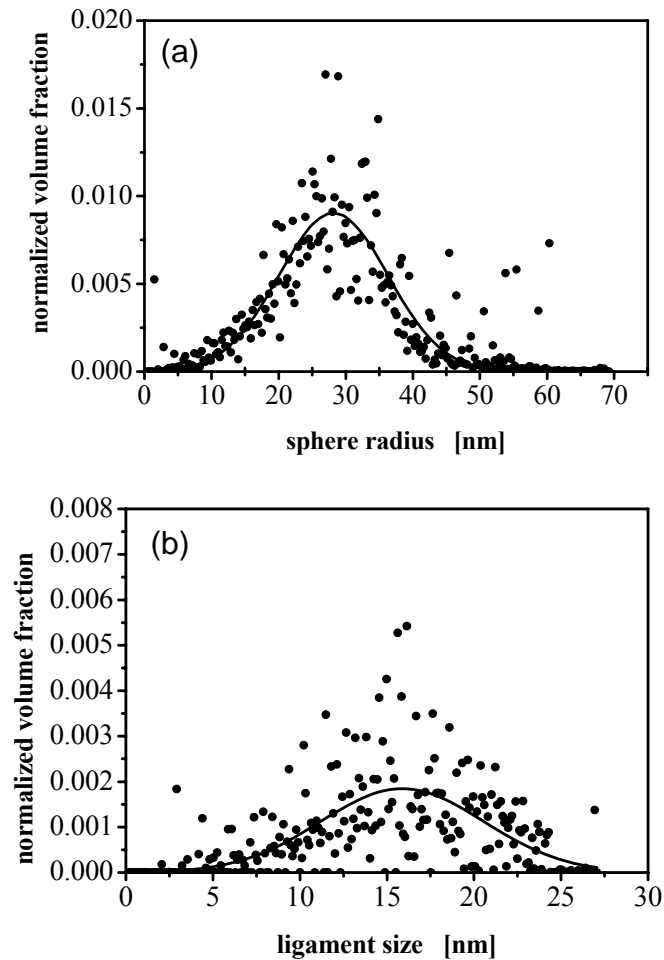


Figure 4.8 a) Quantification of the pore sizes in terms of granulometry distribution as described in the text [12]. The solid line shows a Gaussian fit centred at a pore radius of 28 nm. b) Pore size distribution as described in main text. Solid line shows a Gaussian fit, ignoring the data point at size < 2nm. This fit reveals a mean ligament size of 16 nm.

4.5.3 Net specific surface area

The net specific surface area obtained by counting all surfaces irrespective of their orientation per volume of the sample (pores and solid phase) is $\alpha = 56 \pm 1 / \mu\text{m}$. This is noticeably larger than what would be expected for an estimate based on the characteristic ligament size calculated above and pore fraction: long cylindrical objects of radius r packed at a volume fraction q have $\alpha = 2q/r$. Using $q = 0.24$ and $r = 16\text{nm}$, $\alpha = 30 / \mu\text{m}$, which is only about half of the actual value obtained above. Similar discrepancies are common in structures with a wide distribution of feature sizes, in particular when the different measures for the size are based on different moments of the distributions. This emphasizes the inconsistency in using a single measure of size for characterizing the structure, and the need for a more differentiated analysis such as the one presented here.

4.5.4 Surface orientation distribution

The surface orientation distribution function $S_V(\mathbf{n})$ provides one of several measures for microstructural anisotropy [13,14]. In a sample with the volume V , the total area of surface with its normal oriented within the solid angle $d\Omega$ about the unit vector \mathbf{n} is $S_V(\mathbf{n}) V d\Omega$. MAVI [12] computes S_V by analysing a transform of the original binary image, which is obtained by labelling each voxel according to the occupancy (solid or pore) of the neighbouring voxels. Associated with the elements of the discrete set of possible neighbourhood configurations are 26 discrete surface orientations, with \mathbf{n} along the edges, face- and space diagonals of a voxel [16]. We present here the values of S_V for three orthogonal directions, namely the set of voxel edges x and y (in the plane of the foil) as well as z (out of plane). The respective values are $S_x = 3.9\mu\text{m}^{-1}\text{sr}^{-1}$, $S_y = 6.3\mu\text{m}^{-1}\text{sr}^{-1}$, $S_z = 0.9\mu\text{m}^{-1}\text{sr}^{-1}$. While the uncertainty in this data is unknown, the trend agrees with what can be seen in figures 3.5, where many ligaments appear elliptical in cross-section, with the long axis of the ellipse aligned preferentially with the sample (foil-) normal. Thus, surface orientations with their normal in the plane of the foil may be noticeably more frequent than those with a perpendicular orientation. The anisotropy may relate to the corrosion direction, which is presumably normal to the surface. However, the anisotropy developing during coarsening cannot be excluded, which may also be influenced by the presence of the macroscopic sample surface.

The net specific surface area (per volume of the ligaments) governs the surface-induced pressure [15]. When the surface orientation distribution function is anisotropic, then the volumetric mean of the stress tensor is anisotropic [5]. Assuming a uniform and isotropic surface stress, the volumetric mean of the surface-induced stress is here expected to be largest in the direction normal to the foil.

4.5.5 Mean curvature

The local value of the mean curvature, κ , which is the sum of the inverse values of the principal radii, at a given point on the surface is an important parameter, since gradients in κ provide driving forces for transport of matter that leads to coarsening. The mean curvature is also important for the local value of the normal component of the surface-induced stress underneath the surface of the ligaments [16]. The analysis provided an average value of the mean curvature, $\langle\kappa\rangle$, defined as the integral of κ over the surface, divided by the total surface area, $\langle\kappa\rangle = 55/\mu\text{m}$. The surface normal was oriented outwards as seen from the solid phase. Although it is too simplistic approach to reduce a complicated microstructure like that of npg to simple geometrical shapes, it may be instructive to compare the experimental value of $\langle\kappa\rangle$ with that of idealized, cylindrical ligaments of radius $r = 16 \text{ nm}$ (which is the mean ligament size deduced from the pore size distribution shown in figure 4.8 b). For such cylinders the calculated value of κ is $62.5/\mu\text{m}$, which is close to the actual value obtained from above analysis.

This excellent agreement suggests that, though there are many saddle-point like features where the principal radii of curvature are of opposite sign, the solid phase has essentially a convex surface. Thus, on average, compressive normal stresses are expected near the surface if the surface stress is positive.

4.6 Conclusion

The most important observations obtained using TEM tomography are: i) The structure represents a contiguous network of branched ligaments. ii) The structure is quite inhomogeneous, with a broad distribution of ligament and pore diameters and shapes. iii) As a consequence, the specific surface area is larger than what would be estimated based on the characteristic ligaments size. iv) In spite of presence of many saddle-points like features, the average mean curvature is positive and close to that expected for a convex objects of the size of the ligament diameter. v) Encased voids are observed within the ligaments; there is no obvious explanation for the formation of these features.

The results discussed above highlight the potential of tomographic reconstruction from transmission electron microscopy images to determine the complex micro-morphology of a sample as npg. The reconstruction allows visualization of the shape and size of the microstructural elements as well as their topology in 3-D. The technique appears particularly powerful when combined with 3-D stereological analysis. In this way, quantitative information may be obtained for various microstructural parameters (for instance, volume fraction of the phases, feature size distributions, and specific surface area) that control the material's performance in various applications.

References

-
- [1] A.J. Forty, P. Durkin, *Phil. Mag. A* 42 (1980) 295.
 - [2] B.G. Ateya, G. Geh, A.H. Carim, H.W. Pickering, *J. Electrochem. Soc.* 149 (2002) B27.
 - [3] A.M. Hodge, J. Biener, L.L. Hsiung, Y.M. Wang, A.V. Hamza, and J.H. Satcher, Jr., *J. Mater. Res.*, 20 (2005) 554
 - [4] S. Parida, D. Kramer, C. A. Volkert, H. Rösner, J. Erlebacher and J. Weissmüller, *Phys. Rev. Lett.* 97 (2006) 035504.
 - [5] C. A. Volkert, E. T. Lilleodden, D. Kramer, J. Weissmüller, *Appl. Phys. Lett.* 89 (2006) 061920.

-
- [6] A. M. Hodge, J. Biener, L. L. Hsiung, Y. M. Wang, A. V. Hamza, and J. H. Satcher, *J. Mater. Res.* 20 (2005) 554.
- [7] D. Lee, X. Wei, X. Chen, M. Zhao, S. C. Jun, J. Hone, E. G. Herbert, W. C. Oliverd and J. W. Kysar, *Scripta Mater.* 6 (2007) 437.
- [8] G. Mason, *J. Colloid Interface Sci.* 32 (1970) 172.
- [9] <http://www.itwm.fhg.de/mab/projects/MAVI/>.
- [10] P. Soille, in *Morphological Image Analysis*, Springer, Berlin 1999.
- [11] L. J. Gibson and M. F. Ashby, in *Cellular Solids: Structure and Properties*, Pergamon, Oxford 1988.
- [12] J. Biener, A. M. Hodge, and A. V. Hamza, *Appl. Phys. Lett.* 87 (2005) 121908.
- [13] J. Ohser and F. Mücklich, in *Statistical Analysis of Microstructures in Materials Science*, John Wiley & Sons, Chichester 2000, Ch. 3.-4.
- [14] J. E. Hilliard, *Trans. AIME* 224 (1962) 1201.
- [15] J. Weissmüller and J. W. Cahn, *Acta mater.* 45 (1997) 1899.
- [16] M. E. Gurtin, *Arch. Rat. Mech. Anal.* 131 (1995) 67.

Chapter 5: Self-deformation: Effect of the dealloying rate

5.1 Introduction

During our studies of the dealloying process, we observed a macroscopic volume shrinkage by more than 20 volume-percent. The observations might seem expected, since dealloying removes more than half the atoms from the solid solution. Yet, the finding is actually not immediately compatible with models of dealloying, such as that of Refs. [1] and [2], as it describes the dealloying process as the diffusive rearrangement of Au adatoms and vacancies, created after the dissolution of the less noble atoms (e.g. Ag). On a rigid lattice, interchange of the components (Au and vacancy) on the neighboring lattice sites would keep the external dimension of the sample unchanged during dealloying (see Sec.5.3). It is found out that the phenomena can be related to several microscopic processes occurring during dealloying. Discussion of such processes and their interrelation is the subject of the present chapter.

5.2 Results

5.2.1 Insitu dealloying of $\text{Ag}_{1-x}\text{Au}_x$ alloys

In our experiment, the volume shrinkage during dealloying was always observed in several alloys and compositions. An example of such dimension changes in cubes (about 1mm each side) of bulk $\text{Ag}_{75}\text{Au}_{25}$, investigated in-situ during potentiostatic dealloying in a dilatometer is presented in part “a” of the figure 5.1. In this typical case the variation of lateral strain and charge with dealloying time is presented in figure 5.1a. The strain was calculated by dividing net lateral length change with the original length,

l_0 . From the figure, variation of both dealloying charge (calculated by integrating dealloying current) and strain change seems to exhibit nearly same trend with dealloying time. It is more apparent from figure 5.1b that the strain during dealloying varies roughly in proportion to the charge transferred and, therefore, to the amount of Ag removed. The total lateral strain ($\Delta l/l_0$) produced in this sample is about 7.3%. As the sample of figure 5.1 is macroscopically isotropic; the net lateral contraction of 7.3% after complete dealloying suggests a net volume reduction by as much as 20%.

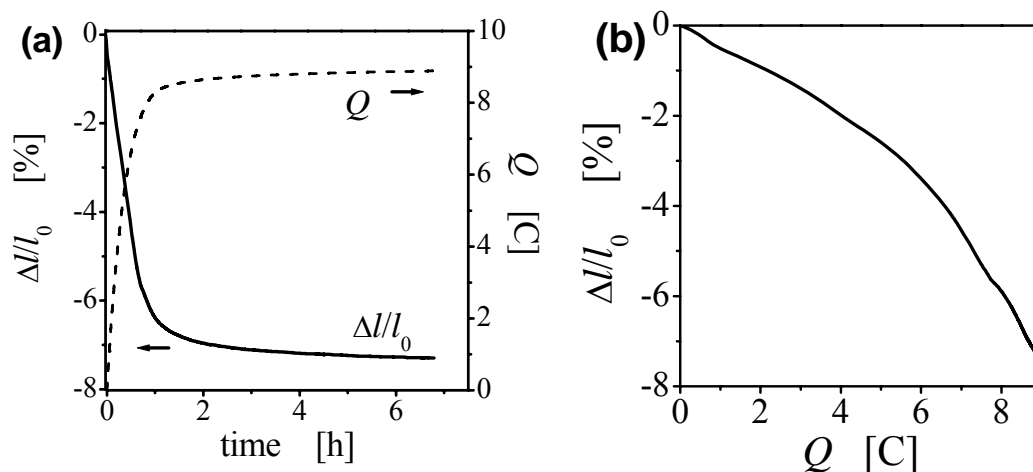


Figure 5.1 (a): In-situ dilatometry traces for bulk (1 mm edge-length cubes) $\text{Ag}_{75}\text{Au}_{25}$ showing time-evolution of relative length change $\Delta l/l_0$ and of transferred charge Q at dealloying potential 850 mV versus Ag/AgCl. (b) $\Delta l/l_0$ versus Q for the data in (a).

The effect of dealloying on sample dimension in case of thin gold leaf samples were studied by comparing digital pictures taken before and after dealloying. Compared to bulks samples, the leaf samples are thinner by order of 10^4 . Figure 5.2 shows photographs of a 6 carat gold leaf sample (120nm thick and original length of ca.23mm each side) before and after dealloying in 1M HClO_4 at 1V. The vertical and horizontal edge lengths are seen to shorten by about 4.5 and 3mm, respectively, i.e. reduced 20 and 13% of the original length, which translates into the overall macroscopic surface area reduction by 30%.

By EDX analysis Ag fractions in dealloyed samples was found to vary between 4 to 10 at-%, indicating the removal of most of the Ag during dealloying. Also, from the EDX analysis, the deposit at the counter electrode was found to be mostly Ag with ≤ 0.2 at-% Au, confirming that Au does not dissolve under the conditions of the experiments. By optical microscopy it was verified that the dilatometer pushrod does not indent the bulk nanoporous sample surface, and that the npg samples are free of cracks at the scale of microns or above.

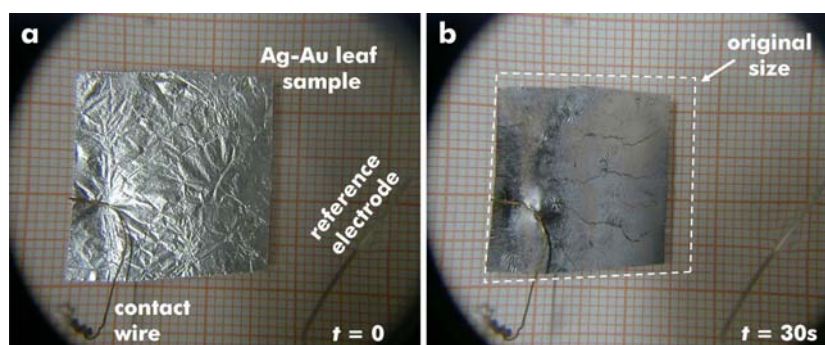


Figure 5.2: Photographs of 6 carat ($\text{Ag}_{80}\text{Au}_{20}$) leaf sample before (a) and after (b) dealloying in 1M HClO_4 at 1V, showing area reduction by about 23%. Leaf is floating on electrolyte; ring-shaped counter electrode is located outside the image area. As noted in the picture it took about 30s to complete the dealloying at the given potential.

5.2.2 Extent of dealloying shrinkage vs. rate of dealloying

It was observed that dealloying of $\text{Ag}_{1-x}\text{Au}_x$ alloys at any potential above the critical potential of dealloying, results in volume shrinkage. The extent shrinkage depends on the potential applied (E_D) for dealloying and hence on the rate of dealloying. Therefore, dealloying was performed at various potentials, in order find a correlation between extent of shrinkage and the rate of dealloying

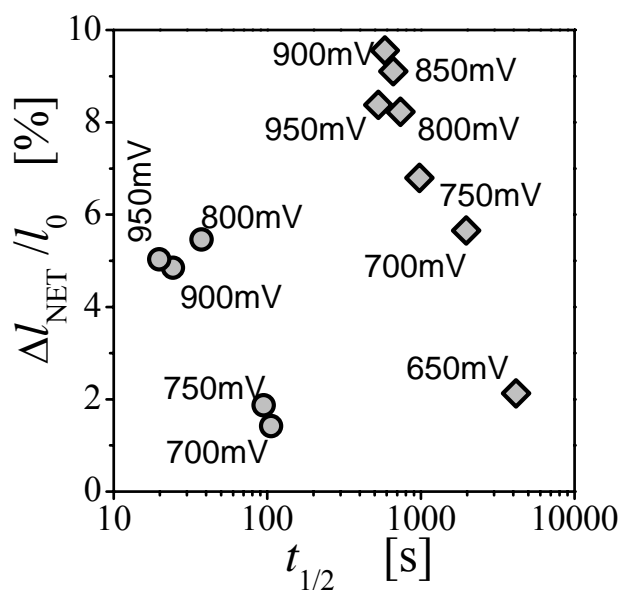


Figure 5.3: Net length change (normalized to original lengths) after completion of dealloying versus the half-time ($t_{1/2}$) of dealloying for bulk (◆, $\text{Ag}_{75}\text{Au}_{25}$) and leaf (●; 11 carat, $\text{Ag}_{67}\text{Au}_{33}$) samples. Data points are labelled according to applied potential.

In Figure 5.3, net length change of bulk $\text{Ag}_{75}\text{Au}_{25}$ alloy and the thin 11 carat gold leaf samples (of composition $\text{Ag}_{67}\text{Au}_{33}$) dealloyed at various E_D in 1M HClO_4 , is plotted with respect to a characteristic time, $t_{1/2}$. This parameter represents the time at

which half of the total dealloying charge was transferred. From the figure, the extent of shrinkage is larger and dealloying is faster (with lesser $t_{1/2}$) at higher E_D . Thus, for bulk as well as gold leaf samples there is a correlation between the net lateral shrinkage and the dealloying rate. Also from the figure, the amount of lateral shrinkage in the 11 carat leaf is less than that for the bulk material, which may be due to the higher Au fraction in the former sample. Still the net lateral strain in the leaf sample is significant.

5.2.3 E_D and defect in microstructure: TEM observations

The samples dealloyed at different E_D were found to have microstructures containing different structure size and different type and density of defects. Figure 5.4a represents a bright field TEM micrograph of npg obtained by dealloying 6 carat gold leaf samples in 1M HClO₄ at $E_D = 600$ mV. The average ligament size in the micrograph is about 20 nm. In the microstructure of npg obtained at 850mV (Fig.5.4b), the average ligament size is about 4nm. Thus it is found that the characteristic ligament size drops with increasing E_D , i.e. from 20nm at 600mV to 4 nm for the sample dealloyed at 850mV. The micrograph of npg obtained at lower E_D , 600mV (Fig.5.4a) appears much more open, with larger and wider pores, and hence of lower density as compared to that shown in Figure 5.4b.

Figure 5.4c represents the high resolution TEM micrograph of sample dealloyed at 600mV. The micrograph displays a coherent defect-free lattice, with continuous lattice fringes. However for the sample dealloyed at higher potential e.g. 850mV, high resolution TEM show higher density of defects of various nature, as exemplified in figure 5.4 d & e. In figure 5.4d very large density of defects, like lattice dislocations, stacking faults and twins, are apparent. An unusual defect features found in microstructure of the sample dealloyed at higher E_D , (Fig.5.4e) are the missing lattice planes associated with pores. Counting the {111}-lattice fringes on opposite sides of pores reveals a deficit of more than one lattice spacing. Though rarely, high angle grain boundaries are occasionally found in micrograph of sample dealloyed at higher E_D , such as in Fig. 5.4b (pointed by an arrow). While the limited statistics of the observations prevents quantifying the defect density, there is a clear trend for more defects at higher E_D .

Because of channelling contrast in focussed ion beam (FIB) microscopy it is possible to observe grain structure in a crystalline material. The FIB microscopy (shown in Fig.5.4f) of npg obtained by dealloying bulk Ag₇₅Au₂₅ shows larger grains of 50–100 μ m [3]. Given, the existence of such larger grain, the entire frame of observation as shown in Fig. 5.4e is a single grain, which supports the view of the conservation of the larger grain size of the master alloy during dealloying.

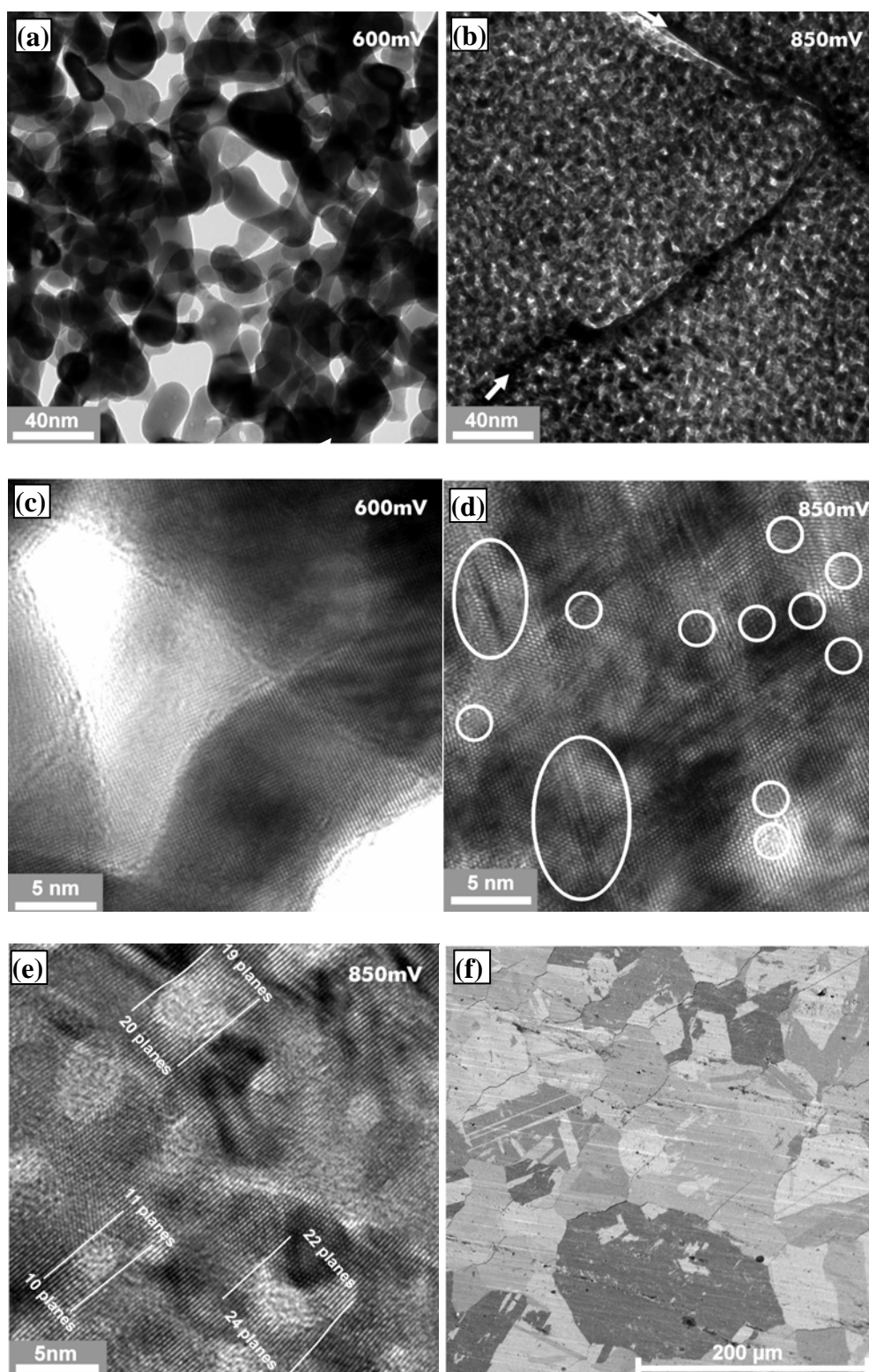


Figure 5.4: Micrographs of nanoporous gold (npg) obtained by dealloying of 6 carat gold leaf in 1M HClO₄. Bright-field transmission electron micrographs of npg dealloyed at **a)** 600mV, **b)** 850mV. The arrow in **b)** marks a high-angle grain boundary; **c)** HRTEM of npg dealloyed at 600mV; **d)** HRTEM of npg at dealloyed at 850mV showing a selection of lattice dislocations and stacking faults marked by circles and ellipses, respectively; **e)** High-resolution transmission electron micrographs (HRTEM) of npg at dealloyed at 850mV, showing some lattice planes end in pores. **f)** FIB microscope image of npg obtained by dealloying Ag₇₅Au₂₅ alloy.

5.2.4 Dealloying shrinkage vs. composition: Pt addition

It was observed that addition of increasing amount of Pt in $\text{Ag}_{1-x}\text{Au}_x$ composition reduces the amount of shrinkage during dealloying. Figure 5.5a represents a plot of net lateral shrinkage in various compositions of $\text{Ag}_{1-x-y}\text{Au}_x\text{Pt}_y$ with atomic percent of Pt in the starting composition, which shows a tendency towards lesser shrinkage with higher Pt atomic percent in the starting composition. Also, as shown in Fig.5.5b, the characteristic half time, $t_{1/2}$, increases with increasing amount of Pt in the alloy.

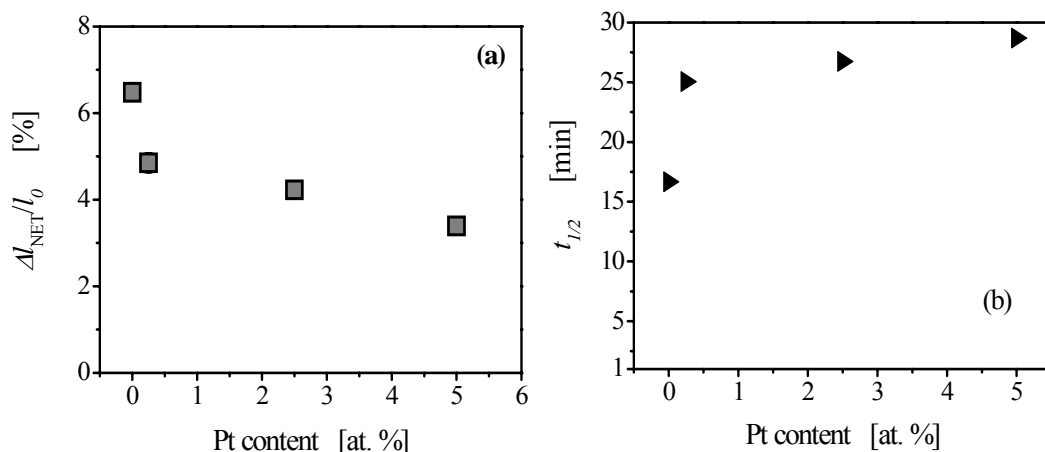


Figure 5.5: (a) Net dealloying strain (■) at various Pt content in $\text{Ag}_{1-x-y}\text{Au}_x\text{Pt}_y$ alloy, where Ag content is fixed at 75 at % and $y_{\text{Pt}} = 0.25, 2.5$ and 5 at.%. Zero at.% of Pt represents shrinkage of $\text{Ag}_{75}\text{Au}_{25}$ alloy. All samples were of comparable size (ca.1.9mm) and were dealloyed in 1M HClO_4 and at $E_D = 0.85\text{V}$; (b) The half time, $t_{1/2}$, (►) representing the time at which half of the total dealloying charge was transferred for a given composition.

For comparison, the lateral shrinkage during dealloying of $\text{Ag}_{1-x}\text{Au}_x$ alloy is also given in the figure as the data for zero at.% of Pt. It can be seen that there is a marked effect of the Pt addition on dealloying shrinkage. In all composition the Ag content was fixed at 75 at. % and all the samples studied are of comparable lateral dimension. All samples were dealloyed in 1M HClO_4 at 850mV, which took about six and half hours for completion.

5.2.5 Shrinkage during electroless dealloying

As discussed above, under potentiostatic conditions of dealloying, $\text{Ag}_{1-x-y}\text{Au}_x\text{Pt}_y$ and $\text{Ag}_{1-x}\text{Au}_x$ alloys undergo volume contraction. Under potentiostatic condition, the rate of dealloying can be controlled via the applied potential, which also has an influence on the final structure size evolved after dealloying (see Sec.5.2.3). Dealloying can also be carried out by just exposing Ag-Au alloy to a strongly oxidizing solution, which does not require application of a potential (i.e. electroless dealloying). In this case there is no control over the rate of dealloying. Therefore, it is imperative to check what

happens to the overall dimension of the alloy sample if dealloying is carried out in the strong oxidizing acid, such as 65% concentrated HNO_3 . Figure 5.6 represents net lateral strain produced in $\text{Ag}_{75}\text{Au}_{25}$ alloy, when dealloyed in 65% concentrated HNO_3 . Even under this condition the lateral shrinkage during dealloying is significant, at about 8% and the process continues for a long time span. From the figure, the sample still shows the tendency of shrinkage, even towards the end of the process (i.e after ca. 18 hours).

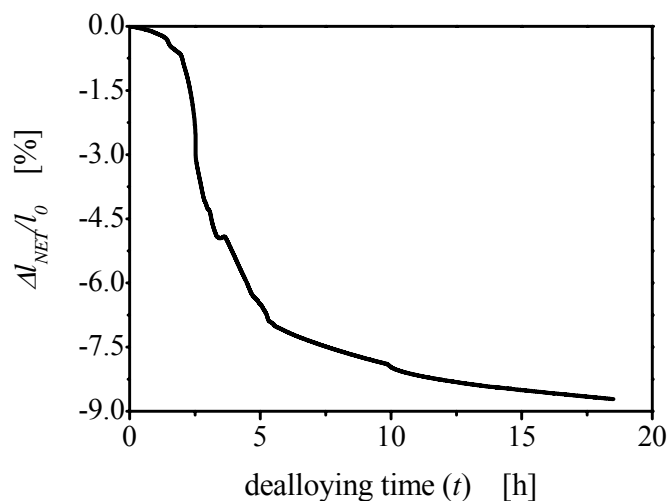


Figure 5.6: Variation on net lateral strain with dealloying time in electroless dealloying of $\text{Ag}_{75}\text{Au}_{25}$ alloy in 65% concentrated HNO_3 .

5.3 Discussion and conclusion

For various npg samples EDX indicates that Ag fractions after dealloying vary between 4 and 10 at-%, depending on the dealloying time. This supports the notion that most of the silver in the alloy is removed during dealloying. Lattice parameter refinements from x-ray diffraction of 6 carat leaf sample (sec.4.2, chapter 4) yield $a = 408.0(1)$ and $406.9(1)$ pm for master alloy and porous Au, at a residual Ag fraction of 6 at-%. This reduction, by 0.3 %, of lattice constant, is consistent with the somewhat lesser lattice parameter of Au as compared to Ag. Thus, the relative volume change due to the variation of the lattice parameter is of the order of -1%, which is negligible in comparison to much larger macroscopic dimension changes found in in-situ dealloying of bulk and leaf sample.

At first sight, the observations of a reduction in the outer sample dimensions may not be surprising in view of the fact that dealloying removes more than half the atoms from the solid solution. Yet, the finding is actually not immediately compatible with models of dealloying, such as that of Refs. 4 and 5, which work with a rigid lattice: It is compatible with such models to consider a coherent lattice extending throughout both the solid phase and the pore space of npg, pores being viewed as clusters of lattice sites

occupied by vacancies, and only two elementary steps are considered, i) dissolution, that is, switching the occupancy of a single lattice site from ‘Ag’ to ‘vacancy’, and ii), diffusion, that is, interchanging components (Au and vacancy) on neighbouring lattice sites. On a rigid lattice these are local processes which leave the external dimensions of the body invariant, a statement which holds even if one of the components consists of vacancies.

As a notable exception to the above statement, the external surface will recede by one interplanar spacing every time the outermost lattice plane is removed by transport of Au atoms from that surface into the interior of the porous layer. In view of the unusually large surface diffusion coefficient of Au at the metal-electrolyte interface (see references in Ref. 5) this might appear to be the most obvious shrinkage mechanism in the very first stages of dealloying, when the dissolution occurs near the macroscopic sample surface. However, as the dissolution front propagates into the bulk, the diffusion distance to the surface increases, hence the rate of transport should diminish and shrinkage eventually come to a halt for sufficiently deep dealloying. The observations of very similar amounts of shrinkage in leaf and bulk samples, in spite of almost four orders of magnitude difference in thickness, as well as the continued shrinkage in the bulk sample even at the very end of the dissolution, when the dealloying front has moved hundreds of microns below the sample surface, argue against this explanation. Furthermore, the large *lateral* shrinkage observed in Au leaf cannot be explained by the condensation of vacancies at its surface, which would only reduce the thickness.

In addition to the above concerns, there exists a problem of identifying a driving force for long-range transport of matter between surface and underlying porous layer. Curvature-driven coarsening is based on transport of matter from positively curved regions on the surface to negatively curved ones. Since the ligaments exhibit saddle-point like features with highly nonuniform values of the mean curvature, coarsening is expected to proceed predominately by local transport on the scale of the ligament length (order of 10nm) rather than by long-range transport to the outer surface (up to hundreds of microns). Thus, curvature-driven surface diffusion is likely not the mechanism leading to shrinkage. By a similar argument, grain boundaries can be ruled out as sinks for vacancies: due to the large grain size, the transport distance is too large.

As discussed above diffusion can not be the sole mechanism of shrinkage observed. Also elastic distortion can be ruled out, given the insignificant change in lattice parameter found from x-ray diffraction observations. Therefore, it appears that plastic deformation mechanisms need to be taken into consideration. While this notion is supported by observation of increasing defect density at higher E_D , correlating with the increasing shrinkage, none of the processes discussed below has been confirmed.

The idea of ligament shear touches on an issue of great interest in nanomechanics: in small cylindrical bodies the surface-induced stress is not hydrostatic [6]. In a recent atomistic simulation result [7] it is revealed that there exist a critical surface stress-induced mean pressure above which the pore structures collapse causing

plastic deformation in the nanoporous structure. Dislocation-mediated shear would require dislocation nucleation, which is an unresolved issue in nanostructures [8] and simulations of tensile loading suggest a transition from dislocation nucleation to homogeneous slip at a ligament diameter of ~ 1.5 nm [9]. In any case, surface stress-induced compressive yielding is expected to occur only in ligaments with diameters of several nanometers or less [10]. Although this diameter is rather smaller than that observed ex-situ (see Fig. 5.4a and Fig.4.3 in Chapter4), it is conceivable that such small diameter ligaments exist as a transient state, subject to rapid coarsening.

All attempts at rationalizing the shrinkage in terms of dislocations appear to require a mechanism for the formation of dislocations, since a large number of these defects are required to explain the large shrinkage. The injection, at the dissolution front, of lattice vacancies or di-vacancies [11] into the bulk and their subsequent clustering to form dislocation loops is fraught with controversy [12,13,14,15] and should be considered with caution. The vacancies injection mechanism requires: sufficiently large dealloying potential to enable the dissolution of terrace atoms rather than kink or step atoms, the subsequent burial of the terrace vacancies formed, and the fast motion of the ensuing bulk vacancies. A more plausible process, explaining observations in Fig.5.4e, is that sufficiently small pores could collapse to form a planar crystallographic fault bounded by a dislocation loop, reducing their net surface energy in favour of the strain energy of the loop, similar to the collapse of vacancy clusters in bulk crystals [16]. The observation of closed pores or voids of about 1-5 nm size within the ligaments as shown Fig. 4.4 & 4.6 in chapter 4, could be due to one of the above reason discussed. The propagation of dealloying requires open porosity for access of the electrolyte to the dealloying front and hence is not expected to directly create closed pores. It is also not obvious how ligament coarsening can result in porosity, since the fundamental process would seem to widen existing pores rather than create new ones.

All processes considered above become more likely as the dissolution rate increases since this drives the surface at the dealloying front further away from equilibrium, thereby decreasing the ligament and pore sizes (cf. Fig. 5.4a and Sec. 5.2.3). This notion agrees with the observation of more shrinkage at faster dissolution in the bulk and leaf samples.

It is expected that the processes at the dealloying front depend on the electrode potential not only through the dissolution rate but also through the dependency of formation enthalpy and diffusion constants of surface adatoms and surface vacancies on the electrode potential. The issue is intricately linked to the adsorption of hydroxide at positive electrode potentials. In this respect it is noteworthy that the shrinkage is indeed reduced at lesser potential, where hydroxide adsorption is weak. It is also significant that considerable shrinkage is observed throughout the entire potential range studied, indicating that the observation may be relevant for the 'typical' conditions of dealloying experiments, which will not generally be free of hydroxide adsorption. A detail of this phenomenon will be covered in the next chapter.

The low dealloying shrinkage in Pt-containing alloys as compared to the Ag-Au alloys (Fig.5.5) may be due to the solid solution hardening. The added Pt atoms have their own strain fields in the lattice, which provides an uphill barrier to the mobility of the dislocations. It costs a lot of elastic energy for dislocation to move past Pt atoms, which in turn creates a distortion of the lattice and hence is not favourable.

In summary, our study shows a quite unexpected dimension change during dealloying of Ag-Au in spite of the retention of the crystal lattice structure in that system. We suggest that plastic deformation, which could arise by homogeneous slip in small ligaments or by climb of lattice dislocations, provides the most obvious mechanism.

References

- [1] J. Erlebacher, M. J. Aziz, A. Karma, N. Dimitrov, K. Sieradzki, *Nature* 410 (2001) 450.
- [2] J. Erlebacher, *J. Electrochem. Soc.* 151 (2004) C614.
- [3] S. Parida, D. Kramer, C. A. Volkert, H. Rösner, J. Erlebacher and J. Weissmüller, *Phys. Rev. Lett.* 97 (2006) 035504.
- [4] J. Erlebacher, M. J. Aziz, A. Karma, N. Dimitrov, K. Sieradzki, *Nature* 410 (2001) 450.
- [5] J. Erlebacher, *J. Electrochem. Soc.* 151 (2004) C614.
- [6] J. Weissmüller, J.W. Cahn, *Acta Mater.* 45 (1997), 1899.
- [7] D. Crowson, D. Farkas and S. G. Corcoran, unpublished work.
- [8] J. Weissmüller, J. Markmann, *Adv. Eng. Mater.* 7 (2005), 202.
- [9] M.R. Sørensen, M. Brandbyge, K. W. Jacobsen, *Phys. Rev. B* 57 (1998) 3283.
- [10] J. Diao, K. Gall, M.L. Dunn, *Phys. Rev. B* 70 (2004) 075413
- [11] H. W. Pickering, C. Wagner, *J. Electrochem. Soc.* 114 (1967) 698
- [12] A. V. Vvedenskii, I. K. Marshakov, *Russ. J. Electrochem.* 31 (1995) 234.
- [13] J.-Y. Zou, D.-H. Wang, W.-C. Qiu, *Electrochim. Acta.* 42 (1997) 1733.
- [14] Yu.Ya. Andreev, A.V. Goncharov, *Electrochim. Acta.* 50 (2005) 2629.
- [15] E. Schofield, *Trans. Inst. Metal Finishing* 83 (2005) 35.
- [16] T.L. Davis, *J. Appl. Phys.* 38 (1967), 3756.

Chapter 6: Adsorbate effects on the surface-stress-charge response and surface stress-induced strain in npg electrodes

6.1 Adsorbate effects on the surface-stress-charge response of npg electrodes

When the electrode potential is varied at a nanoporous metal-electrolyte interface, the whole volume of the metal either expands or contracts. This is due to a change in the characteristic parameter namely, the surface stress. The surface stress, f , quantifies the elastic response of the material surface to changes in the bond forces and the electronic structure at the surface. At an electrode surface, f varies as a function of the potential, E , or of the superficial charge density, q . Then, thermodynamic parameter which characterizes the response of f to q is the surface-stress charge coefficient, $\zeta = \partial f / \partial q$ (see Sec.2.2). All recent experiments find that the variation of f with q is linear near the potential of zero charge and all known values of ζ are negative [1,2]. For example, measurement shows, on gold surfaces ζ varies between -1V to -1.5 V [1,4]. In the consequence, metal surfaces tend to expand laterally when charged positively [1, 3, 4].

At present, the microscopic processes linking forces and relaxation at metal surfaces to the surface excess charge density are still poorly understood. Recent density functional theory (DFT) simulations considering of Au cluster ions in vacuum [5] or planar Au surfaces of various crystallographic orientation [6] achieve remarkably good agreement with experiments on metal electrodes in aqueous solutions. Yet, no argu-

ments have emerged so far from these studies that would require ζ to be negative for *all* surfaces. In fact, porous carbons as well as carbon nanotubes exhibit a roughly parabolic variation of the strain with charge, highlighting the importance of the nature of the bonding [7,8].

While investigating the response of the surface-induced stress of npg to surface charging, it was observed that freshly prepared samples exhibit contraction at positive potential and, hence giving an unexpected positive value of ζ . After suitable conditioning, the same samples revert to the conventional behavior, where ζ is negative.

The underlying processes at the npg surface are discussed in regard to the formation of a superficial oxide layer during dealloying. In a parallel study on Pt surfaces, a similar hysteretic behavior at positive potentials is observed, which highlights the role of essentially reversible adsorption at negative potentials [9]. However, the results of Au surface in npg will be elaborated in following sections.

6.1.1 Strategy of the experiment

It was observed that in-situ strain measurements on npg conducted immediately after the synthesis by dealloying gave quite different potential-strain curves compared to samples which had undergone repeated cycling. In an effort to systematically study this phenomenon two types of experiments were performed, the strategies of which are described below.

At highly positive dealloying potential (e.g. $E_D = 850\text{mV}$ vs. Ag/AgCl, in HClO_4) a surface state is formed, which gives an unexpected positive ζ . An initial in-situ strain measurement was designed to explore this state of the surface, which, from now on is called state-I. Again, when potential is scanned extreme cathodic, either in HClO_4 or in NaF solution, an irreversible change of state of the surface occurs, which gives the usual positive ζ . Henceforth the later surface is called as state-II. Care was taken to avoid this irreversible change of surface state in the initial in-situ measurement for state-I; either by restricting the range of potential scans in HClO_4 to potentials close to E_D (called *experiment 1*), or by scanning in NaF (called *experiment 2*). Subsequently, the in-situ strain was measured in state-II, in respective solutions, and the results were compared to those of the initial (state-I), in the same solution.

The experimental set up for in-situ dilatometry is as explained in Chapter 3. In both experiments, HClO_4 solution was used to dealloy the sample. The dealloying was carried out as explained in Sec.3.2.1. The sample remained in place during the entire sequence of measurements. Extensive washing and frequent replacement of the electrolyte was carried out with the intention of minimizing redeposition of Ag and cross-contamination when changing electrolytes.

6.1.2 Results of experiment 1

Here, all the measurements were performed in 1M HClO₄.

6.1.2.1 Strain-charge response in state-I

The graphs in Fig.6.1 refer to scans taken immediately after dealloying i.e. in state-I. The cyclic voltammograms (CV) presented in Fig. 6.1a and the length-versus-charge scans presented in Fig. 6.1b, were probed near the dealloying potential E_D in 1M HClO₄ (scan range about 0.7-1.0V). The voltammogram is featureless and well reproducible, consistent with reversible charging and stable states of the surface. The in-situ strain in Fig.6.1b is plotted with net surface charge, which was calculated by integration of currents in the CV (Fig. 6.1a). The notable observation from strain variation in state-I is that the sample contracts when surface charge is positive.

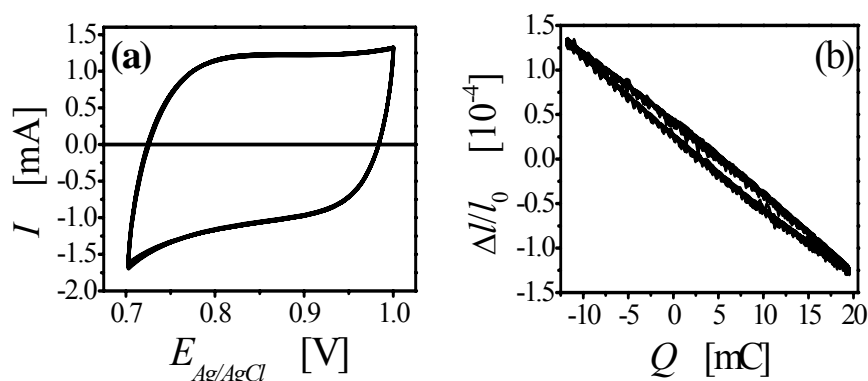


Figure 6.1. Measurements in 1M HClO₄ before cathodic potential sweep, (a) CV in high potential range (0.7V to 1V) at 10mV/s, (b) In-situ strain, $\Delta l/l_0$, versus superficial surface charge measured in potential corresponding to CV as in (a). Q is calculated by integration of current in the CV. All parts show ten successive scans superimposed

6.1.2.2 Cathodic potential sweep and extent of adsorbate coverage

After probing state-I in 1M HClO₄, the potential was swept cathodic. Fig. 6.2a shows the series of fifteen successive cathodic potential scans carried out in 1M HClO₄. The first scan was started at E_D scanning initially towards positive E up to 1V and then towards negative up to 0.01V.

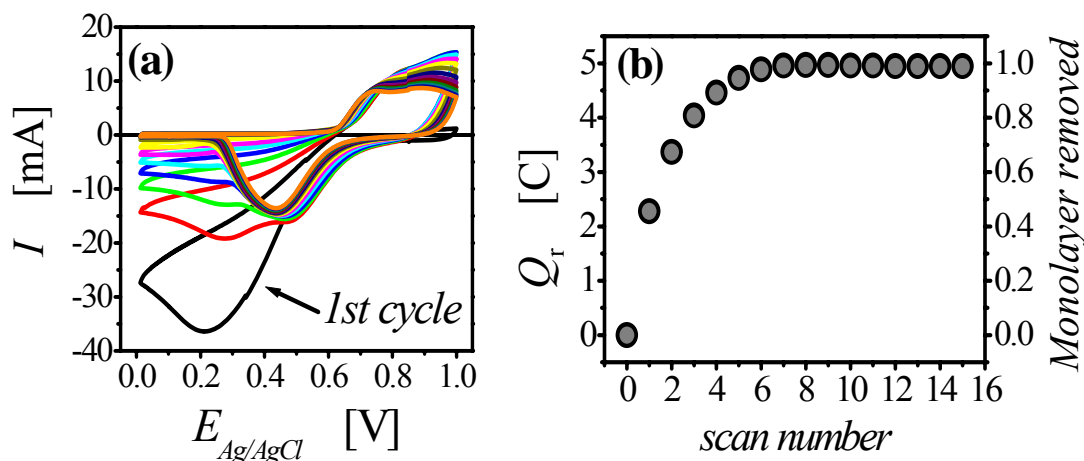


Figure 6.2. Cathodic potential sweep in 1M HClO₄, (a) cathodic potential sweep (15 cycles) in 1V up to 0.01 V potential window at 10mV/s, (b) cumulative charge transferred, Q_r , at the end of each scan (left) and monolayer of oxygen removed (right) after each cycle calculated from Q_r .

The behavior is initially indicative of OH-adsorption. An important anion desorption peak develops during the cathodic part of the first scan, as evidenced by the negative value of the current, I . The negative I persists through a major part of the anodic part of the scan, indicating that the anion desorption is highly irreversible. The irreversibility is apparent throughout the first seven scans, which gradually evolve towards a more reproducible behavior.

Superimposed to the irreversible feature, the scans indicate the reversible adsorption/ desorption of OH, consistent with the well known reversible behavior of polycrystalline Au surfaces in HClO₄.

The cumulative charge transferred, Q_r , after each cathodic cycle was calculated from the respective CV in Fig.6.2a and is plotted versus scan number in the left axis of Fig. 6.2b. Q_r increases with scan number and saturates after about 6 cycles. The net charge transferred after 15 scans are about 5C. Assuming oxygen as the adsorbed species, the numbers of monolayer of oxygen removed were calculated from the Q_r by using the surface area calculated in Sec.6.1.2.4. About one monolayer of oxygen was removed at the end of 15 cycles.

Thus the state-I was found to be the gold surface covered with one monolayer of oxygen and the removal of that oxygen in cathodic sweeping produces clean gold surface, which is state-II.

6.1.2.3 Strain-charge response in state-II

Figure 6.3 shows cyclic strain behaviors in 1M HClO₄ after cathodic potential sweep, i.e. in state-II. It is seen that the behavior after the cathodic scans differs from that immediately after dealloying (i.e. in state-I). In comparison to Fig.6.1b, the total

charge as well as the strain amplitude shown in Fig.6.3a have decreased after cathodic potential sweeping in HClO₄, roughly by factors of 6 and 20, respectively.

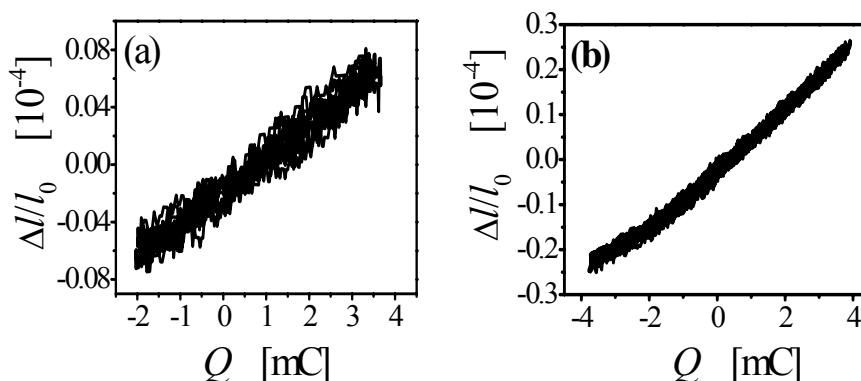


Figure 6.3. In-situ strain versus total surface charge in 1M HClO₄ and 0.3M NaF, measured *after cathodic potential sweep* (Fig. 6.2), (a) strain versus charge measured in 1M HClO₄, in high potential range corresponding to CV as in Fig.1a (+0.7V to +1.05V). The overall slope of strain versus charge is opposite to that in Fig. 6.1b and strain amplitude has decreased by a factor of 20. (b) Strain versus charge measured in capacitive region (-0.3V to +0.4V) in 1M HClO₄. A mostly capacitive potential region in 1M HClO₄ was chosen after measuring the CV at scan rate as low as 5mV/s.

Most importantly, there is a qualitative change in the sign of length-versus-charge graph. Its overall slope changes sign, from contraction during positive potential scans in the as prepared state-I to expansion during same potential scans after the cathodic sweep. The in-situ strain measured in the capacitive region in 1M HClO₄ after the cathodic potential sweep is shown in Fig. 6.3b. In this case, the strain varies linearly with the charge and has a positive slope. The voltammogram in 1M HClO₄ (not shown) is consistent with polycrystalline Au, and the cyclic strain behavior is consistent with previous observations on nanoporous Au, namely a tendency for expansion at positive E [15].

6.1.2.4 Coarsening after cathodic potential sweep

During cathodic potential sweep (sec.6.1.2.2), stripping of oxygen monolayer causes fast diffusion of the Au atom, which results in coarsening on npg. So the pore and ligament size increase and hence, the overall surface area decreases. This effect was probed by measuring the surface area of the sample, in two states described above, as following.

The surface area of the npg electrode in oxygen covered state (state-I) and clean state (state-II) was determined by the capacitance ratio method [10]. In this method, the surface area is calculated by dividing the experimental differential capacitance (C) of npg electrode by double layer capacitance (C_d) of the planner gold surface. To determine C for npg, the CV was recorded at different scan rates (Fig. 6.4a & c). The equation relating the current (I) and the scan rate (v) is given by

$$I = C v = C (dE/dt) \quad (6.1)$$

Then the C was calculated from the slope of linear regression plots of the sums of absolute current vs. scan rate, as shown in Fig. 6.4b & d.

In order to avoid any contribution from charge-transfer reactions, a small potential window of 100mV and constant current regions of the CV were chosen. The sums of the positive and negative currents of each CV were taken at several points to average out any non-ideal polarized electrode behavior.

The experimental differential capacitance, C calculated above is proportional to surface area (A) of our sample, by the relation

$$C = C_d A \quad (6.2)$$

where C_d is the double layer capacitance of the clean Au surface. From impedance measurements [11] C_d at a clean and an oxide covered Au surface was found to be around $40 \mu\text{Fcm}^{-2}$ and $20 \mu\text{Fcm}^{-2}$, respectively. Then the surface area was calculated by dividing the capacitance, C , with C_d . Since state-I is covered with oxygen, for calculation of surface area of npg electrode in this state, value of C_d for an oxide covered Au surface (i.e. $20 \mu\text{Fcm}^{-2}$) was used and for state-II, value of C_d for a planar clean Au surface (i.e. $40 \mu\text{Fcm}^{-2}$) was used.

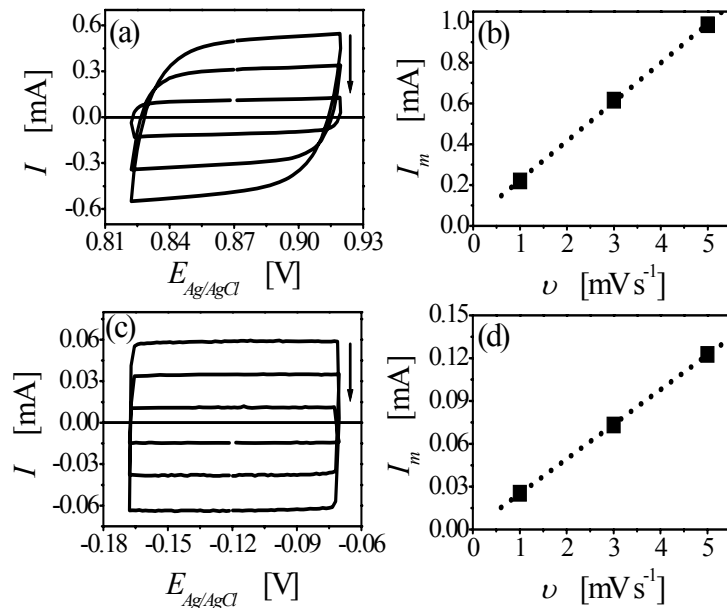


Figure 6.4. Capacitance measurements in small potential range (ca. 100mV) before and after cathodic scan in 1M HClO₄, at different scan rates (v) (a) CV at 5, 3 and 1 mV/s from +0.82V to +0.92V before cathodic sweep (ref. Fig. 6.2), (b) average of absolute current (I_m) at the middle of CVs (solid square) in Fig. 6.4a vs. scan rate, (c) CV at 5, 3 and 1 mV/s from -0.17V to -0.07V after cathodic sweep (ref. Fig. 6.2), (d) average of absolute current (I_m) at the middle of CVs (solid square) in Fig. 6.4c, at different scan rate. Arrows in (a) and (c) indicate direction of decreasing scan rates. Dotted lines in (b) & (d) are linear regression of respective I_m vs. v plots. Slope of I_m vs. v gives the capacitance in respective potential region. Capacitance before cathodic scan is about ten times larger than that after cathodic scan.

Surface area, thus obtained, was normalized with respect to the mass of the sample to obtain the mass specific surface areas, α_m . Thus, the mass specific surface area before and after cathodic scanning was found to be $150 (\pm 5) \text{ m}^2/\text{g}$ and $10 (\pm 2) \text{ m}^2/\text{g}$, respectively.

As seen from CV in Fig. 6.2a, the area under each adsorption/desorption peaks gradually decreases from scan to scan, suggesting that the number of adsorption sites decreases, as would be the case during coarsening of the porous microstructure. This is consistent with the decrease in the surface area of our sample by a factor of ten.

6.1.3 Results of experiment 2

In this experiment npg was obtained by dealloying in 1M HClO₄ at same E_D as in *experiment 1*. But, after dealloying, all further measurements and treatments were carried out in 0.3M NaF. As shown in Fig.6.5a, the strain-to-charge response in state-I was obtained in a wider potential range (-0.2V to +0.9V) and qualitatively similar to that explained under *experiment-1*, but strain amplitude and net charge in 0.3M NaF are larger by factors about ten and four respectively, as compared to those in 1M HClO₄ (shown in Fig.6.1b).

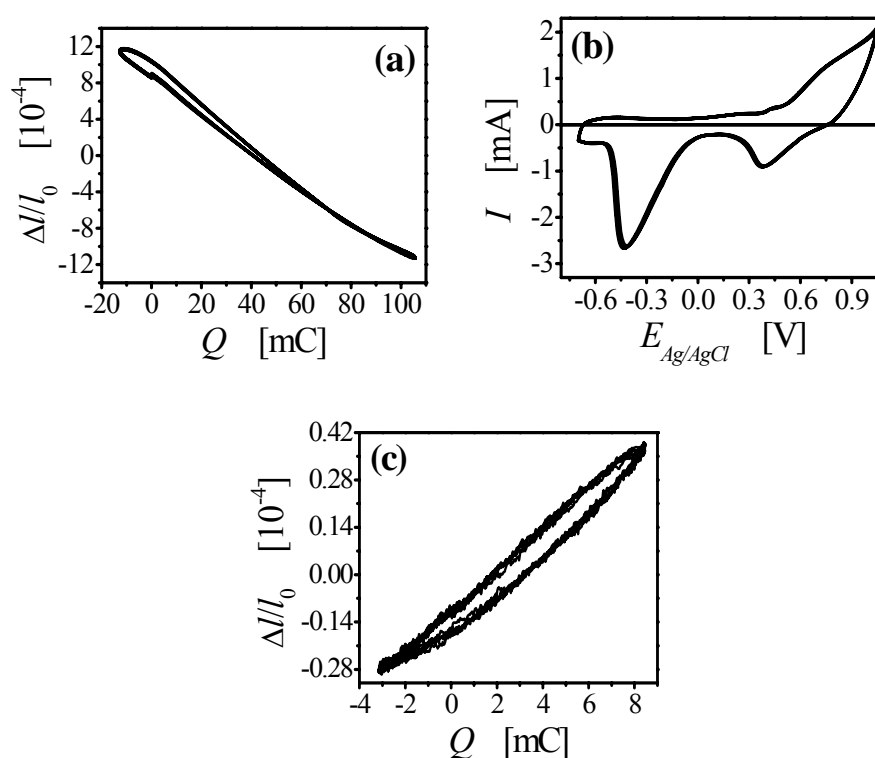


Figure 6.5. (a) In-situ strain, $\Delta l/l_0$, versus superficial surface charge measured by cycling potential at 10mV/s in -0.2V to +0.9V range in 0.3M NaF, before cathodic scan in the same solution. In comparison to data in Fig.1b, strain amplitude is about ten times higher. (b) CV at 10mV/s in a wide potential range (-0.7 to +1.05V) in 0.3M NaF after cathodic scan in the same solution. (c) Strain versus total surface charge measured in capacitive region (-0.6V to +0.2V) in 0.3M NaF, after cathodic potential sweep in the same solution.

After cathodic scanning of the potential in 0.3M NaF, the sign of strain-charge response changes (Fig. 6.5c) to positive as in case of 1M HClO₄. The surface-stress-charge coefficient measured (for derivation see Sec.3.8, Chapter 3) afterwards in capacitive regime in 0.3M NaF, has a value of -1.3V, which is similar to the value obtained in 0.3M NaF after cathodic sweep in 1M HClO₄.

Since the surface-stress-charge coefficient characterize the surface state of the material, its constant values in 0.3M NaF after cathodic scan shows the similar surface state is obtained irrespective of the electrolyte in which the cathodic sweep was carried out.

Efforts have been made to bring the negative strain to charge slope (e.g. state-I) back by either applying a high potential for long time (e.g. at 900 mV in 1M HClO₄ for over 12 hrs) or by cycling potential in oxide formation regime (e.g. 50 cycles between +0.6V to +1.0V in 0.3M NaF, ref. fig. 6.5b). In either case, however, a positive slope was always observed. Application of potential higher than at 1V in 1M HClO₄ results in oxygen evolution.

6.1.4 X-ray diffraction experiment

The npg used here was prepared by dealloying at 0.85V, which is several hundred millivolt above the hydroxide formation peak (see the end cycles in the Fig.6.2a) Therefore, formation of a hydrated oxide layer was probed by x-ray diffraction right after dealloying. Figure 6.6 represents diffraction data of Ag₇₅Au₂₅ alloy before and after dealloying at 0.85V (vs. Ag/AgCl) in 1M HClO₄. The only noticeably change of the diffractograms is a broadening of the Bragg reflections. This broadening can be attributed to the formation of nano-ligaments, which essentially reduces the size of the coherently scattering regions of crystal lattice.

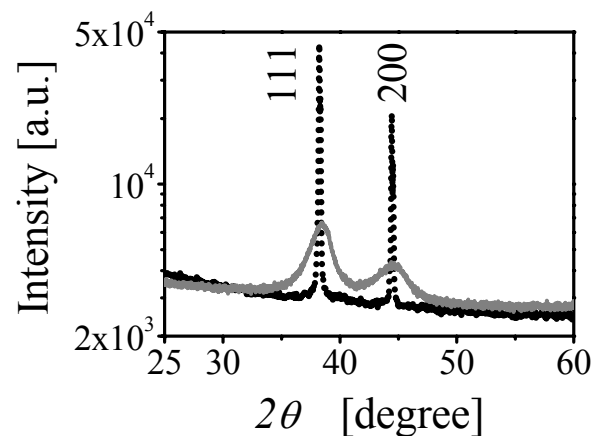


Figure 6.6. X-ray diffractograms of Ag₇₅Au₂₅ alloy before (dotted, deeper shade) and after (solid, lighter shade) dealloying at 0.85V (vs. Ag/AgCl) in 1M HClO₄.

The expected signature of oxidation would have been the appearance of Au₂O₃ diffraction peak at around 30° Bragg angle [12]; however, no extra peaks were found in the diffractograms. Also, there is no significant increase in the diffuse background,

which would indicate an amorphous oxide layer. This might be due to the thin layer (about a monolayer) of oxide layer, which is not detected by x-ray diffraction.

6.1.5 Discussion

The important observations of the previous section can be summarized as follows: immediately after preparation, nanoporous gold samples prepared by electrochemical dealloying tend to contract during anodic potential scans. This behavior is reversible and reproducible; it persists in NaF over wide potential regions, and it also persists in HClO₄ as long as the potential remains within the OH-adsorption region. When the same experiments are repeated after an intermediate cycling to sufficiently large negative potentials in HClO₄ or NaF, the cyclic strain is again highly reversible, but the behavior is now qualitatively different, since the samples tend to expand rather than contract during the anodic part of the scan. The materials behavior in this latter state is consistent with published data for polycrystalline gold and for Au single crystal surfaces, whereas the behavior in the initial state is unusual.

Surface stress-charge coefficient estimate of $\sigma_{\text{p}}/\text{q}$ in its two surface states (state-I & II), obtained before and after the cathodic cycling, was calculated based on the in-situ strain measurements, as is explained in sec.3.8.

From the results of *experiment 1*, in 1M HClO₄ in same potential range (+0.7V to +1V), as in Figs. 6.1b and 6.3a, presenting state-I & II respectively, using $m = 6.33397\text{mg}$ and assuming $\lambda = 1$, the value for ζ obtain as +2.06V before (state-I) and -0.6V after (state-II) cathodic cycling. From cyclic strain change in capacitive regime (-0.3V to +0.4V) in 1M HClO₄ after cathodic scanning (figure 6.3b), one obtains $\zeta = -1.7\text{V}$.

From the results of *experiment 2*, cyclic strain change in capacitive regime (-0.6V to +0.2V) after cathodic scanning in 0.3M NaF, gives $\zeta = -1.3\text{V}$; the same value is obtained in NaF in capacitive range for a sample where cathodic scan is carried out in 1M HClO₄ (*experiment 1*). The values of ζ in different surface states and potential regions are summarized in Table 6.1 below.

There are two significant observations here: i) the values of ζ in the two states of the surface are of opposite sign and ii) the absolute values of ζ are also different for different states of the surface, measured even in the same potential range; and ζ is the same (-1.3V) measured in NaF in the capacitive regime, irrespective of the solution in which cathodic scan was carried out.

Table 6.1: Summary of the values of ζ in different surface states, measured in different potential ranges in different electrolytes.

		Potential range [V]	ζ [V]
<i>Experiment 1</i> (1M HClO ₄)	State-I (oxide covered surface)	+0.7 to +1.0 (Fig.5.1)	+2.06
	State-II (clean surface, after cathodic scan)	+0.7 to +1.0 (Fig.5.3a)	-0.6
		-0.3 to +0.4 (Fig.5.3b)	-1.7
<i>Experiment 2</i> (0.3M NaF)	State-I (oxide covered surface)	-0.2 to +0.9 (Fig.5.5a)	+4.7
	State-II (clean surface, after cathodic scan)	-0.6 to +0.2 (Fig.5.5a)	-1.3
From strain measurement in 0.3M NaF on the clean surface obtained after cathodic scan in 1M HClO ₄		-0.45V to +0.3V (in 0.3M NaF)	-1.3

As discussed in Sec.6.1.2.4, the irreversible desorption of anions occurs with the coarsening of the nanoporous microstructure. The structural coarsening may reduce the reversible strain amplitude but may not change the value and the sign of the surface stress-charge coefficient ζ . According to Eq. (3.2) in Chapter 3, the sign and the value of the ζ is independent of the structure size. Then the observed change of sign and value of ζ must result from a change of state of surface due to surface oxidation, reconstruction, or even roughness.

In fact, the observation of an irreversible negative current in the scans that accompany the change of state of the surface point our attention naturally towards desorption of oxygen anions. Apparently, an oxygen adsorbate layer, which forms during dealloying, is stable under certain conditions, and is desorbed during cathodic cycling HClO₄ or NaF.

The formation of a significant amount of bulk oxide and its subsequent reduction to metallic Au during the cathodic scan would involve the nucleation of new crystallites, refining of the grain size and modifying the crystallographic texture. Our diffraction data along with the retention of structural integrity and the texture argue against the formation of a significant amount of bulk oxide phase during dealloying. The absence of any bulk oxide peak in x-ray diffractograms of dealloyed sample (see Fig.6.6) and the finding of retention of the grain size of the master alloy - of the order of 100 μ m - after dealloying under similar conditions [13] does not support the formation of the bulk oxide.

A remarkable observation is that the voltammograms of the intermediate scan in Fig. 6.2a shows that reversible OH adsorption / desorption peaks are superimposed on the irreversible (oxygen-) anion desorption feature. This, along with the comparative stability of surface state I, argues that the oxide layer in this state is not the same as the OH-adsorbate layer that is reversibly formed in cyclic scan on a clean Au surface (such as scans at end in Fig. 6.2a). In fact, it appears that reversible OH-adsorption may be possible on top of the more strongly bound oxide. This is very much compatible with literature [14].

Single crystal gold surfaces reconstruct sluggishly at strongly negative electrode potential and the reconstruction is readily lifted at positive potential [15]. The surface reconstruction - which couples to the surface stress [16] – may not be a possible reason for the unusual positive ζ . Since neither surface reconstruction is possible at the positive dealloying potential nor would the lifting of reconstruction during the cathodic scan, can be consistent with the known phenomenology. Thus, reconstruction can be ruled out.

Dealloying causes severe surface roughness, due to inherent mechanism of the dealloying process [17]. On a rough surface, step and kink atoms are more energetic due to the reduced number of nearest neighbors than that of a bulk atom. These atoms, having low lattice stabilization energy, possess a higher than average surface energy and surface mobility. Such surface can easily be oxidized under the condition of dealloying.

Also, screening on an oxide covered surface is less efficient than on the clean surface, so that the excess charge can penetrate deeper- a behavior similar to that of semiconductors. The positive-valued ζ might then be understood in terms of filling or depletion of antibonding valence band states during charging at negative or positive potentials on the oxide-covered surface. At negative potential, electrons populate the antibonding valence band, which weakens the bonding between atoms and increases the interatomic distance. This would lead to an expansion of the sample at negative potential. The opposite case of depletion of electron in the antibonding valence band at positive potential strengthens the bonding and reduces bond lengths, and one would expect a contraction of the sample.

6.2 Enhancing the magnitude of the surface stress-induced strain in npg

When in contact with electrolyte, surface diffusion of Au atom is very high depending on applied potential [18]. This often leads to structure coarsening during potential cycling in an electrolyte. Such structure coarsening leads to a significant reduction in the net amplitude of the surface stress-induced strain in npg. For example net amplitude of lateral strain in npg is only 0.015%, as compared to the 0.15% in nanoporous Pt [19].

An example of effect of potential cycling on structure coarsening is presented in Fig. 6.7. From the TEM micrograph of a freshly prepared npg as shown in Fig 6.7a, the structure size is found to be as small as 5 nm. After subjecting to potential cycling the

structure size grow to around 20 nm, as shown in SEM micrograph of such a sample in Fig. 6.7b. This illustrates the coarsening during potential cycling and is consistent with the surface area reduction explained in section Sec 6.1.2.4 before.

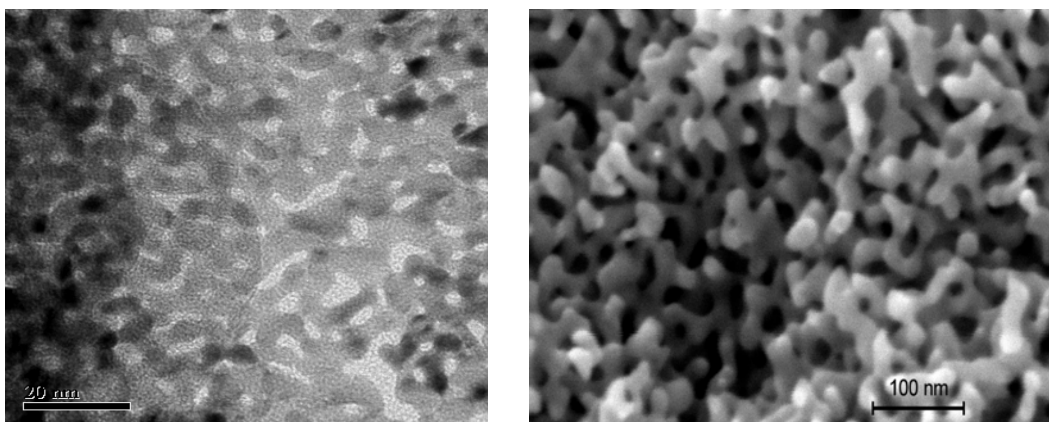


Figure 6.7. (a) Transmission electron micrographs of a freshly prepared npg. (b) SEM micrograph of npg after subjecting to potential cycling in HClO₄. Npg was obtained by dealloying Ag₇₅Au₂₅.

The addition of Pt increases the strain amplitude by stabilizing the structure in npg. As shown in previous chapter (Sec.5.2.4, Chapter 5), the addition of Pt to Ag-Au alloys reduces the volume shrinkage during dealloying. This could be due to the low surface diffusivity of Pt atoms, which is 3-4 orders of magnitude lower than that of Au and/or due to solid solution hardening. The same effect might also lead to formation of stable microstructure with smaller pores and ligaments. Therefore, a series of alloy, Ag₇₅Au_{25-x}Pt_x, was prepared by varying the Pt atomic percent in the original alloys as 1.3 and 2.5 atomic percent, so that the Au-Pt alloy obtained after dealloying as Au₉₅Pt₅ and Au₉₀Pt₁₀, respectively.

Figure 6.8 a-c shows the variation of the net strain ($\Delta L/L_0$, black line, left of each graph) and electrochemical potential (E , red line, right of each graph) with time during ten potential cycles in the given potential region for npg, nanoporous Au₉₅Pt₅ and Au₉₀Pt₁₀ alloys. The strain varies periodically and reversibly as the potential was varied in the given window for respective sample.

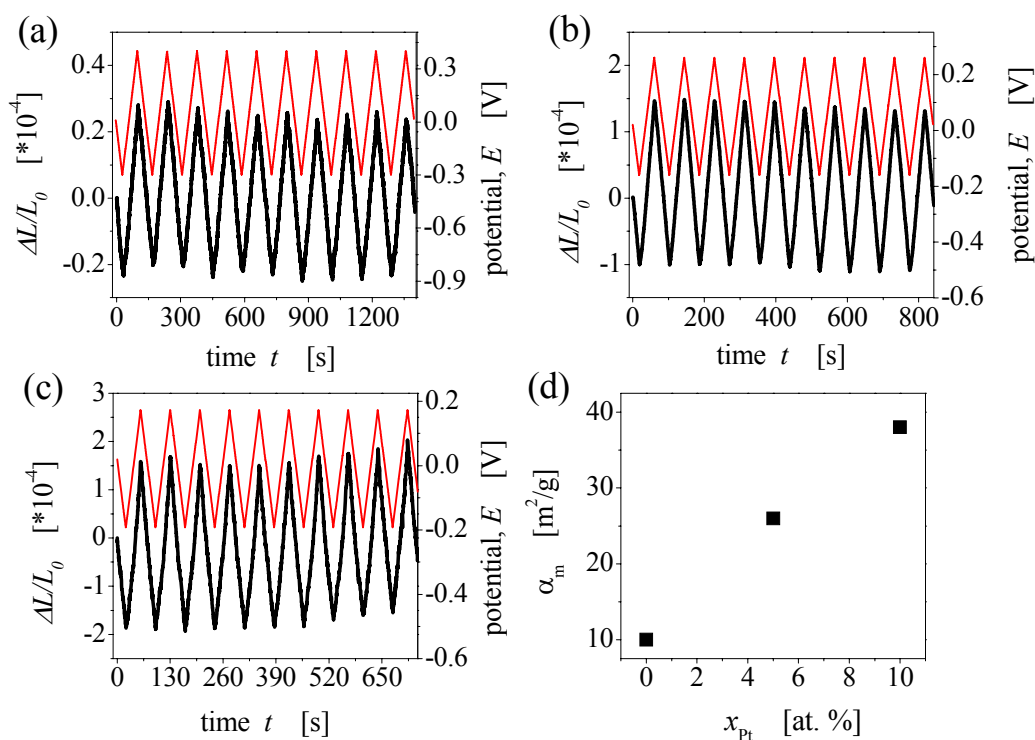


Figure 6.8. Net strain ($\Delta L/L_0$, black line) and electrochemical potential (E , red line) versus time t during 10 successive potential cycles: a) npg dealloyed from $\text{Ag}_{75}\text{Au}_{25}$, b) nanoporous $\text{Au}_{95}\text{Pt}_5$ and c) nanoporous $\text{Au}_{90}\text{Pt}_{10}$, Strain was measured in 1M HClO_4 by cycling potential at 10mV/s, in the potential window indicated. In each case a linear potential window was chosen; d) The mass-specific surface areas (α_m , ■) measured electrochemically versus atomic percent of Pt, x_{Pt} in the nanoporous samples. Zero atomic percent at ($x_{\text{Pt}} = 0$) in “d” corresponds to surface area value for npg.

From the Fig.6.8a, the net strain amplitude in the npg, for the given potential region, is about 0.5×10^{-4} and as shown in Fig.6.8 b & c strain amplitude in the nanoporous $\text{Au}_{95}\text{Pt}_5$ and $\text{Au}_{90}\text{Pt}_{10}$ alloys is 2.5×10^{-4} and 3.5×10^{-4} respectively. This shows that, as compared to npg the net strain amplitude in nanoporous $\text{Au}_{95}\text{Pt}_5$ and $\text{Au}_{90}\text{Pt}_{10}$ alloys increased by a factor of five and seven respectively.

Electrochemical surface area measurement for each nanoporous sample was carried out as discussed in Sec. 6.1.2.4 and is presented in Fig. 6.8d. The mass-specific surface area of corresponding nanoporous sample shows a linear increase with the Pt content in the alloys, which indicate the existence of smaller pores and ligaments in nanoporous Au-Pt samples as compared to npg. Since the surface stress-induced strain in nanoporous metal and alloys is a function of surface charge density, which in turn is a function of “structure size” in the porous body, the existence of smaller structure sizes in nanoporous Au-Pt alloys may be responsible for the increase strain amplitude as compared to npg.

The above results indicate that the nanoporous gold-platinum alloys have an improved stability with respect to the structural growth, which is an important advantage

for actuator applications. The response time is important for an actuator, which determines how fast the sample switches its length in response to the frequency of the potential variation. The response time qualitatively depends on the rate of drift of ion into the pores. This necessitates a systematic microstructural characterization in nanoporous Au-Pt alloys. All these factors leave enough scope for further study in these materials in near future.

References

- [1] W. Haiss, J.-K. Sass, *Langmuir*, 12 (1996) 4311
- [2] N. Vasiljevic, T. Trimble, N. Dimitrov, K. Sieradzki, *Langmuir*, 20 (2004) 6639
- [3] Kramer, D.; Viswanath, R. N.; Weissmüller, J., *Nano Lett.* 5 (2004) 793
- [4] W. Haiss, *Rep. Prog. Phys.* 64, (2001) 591
- [5] F. Weigend, F. Evers, and J. Weissmüller, *Small* 2 (2006), 1497.
- [6] Y. Umeno, C. Elsässer, B. Meyer, P. Gumbsch, M. Nothacker, J. Weissmüller, F. Evers, in preparation. See also preliminary report, Y. Umeno, J. Weissmüller, C. Elsässer, B. Meyer, P. Gumbsch, *Mater. Res. Soc. Symp. Proc.* Vol. 924 (2006) 0924-Z01-09.
- [7] M. Hahn et al., porous graphite.
- [8] Baughman, R. H.; Cui, C.; Zakhidov, A. A.; Iqbal, Z.; Barisci, J.N.; Spinks, G. M.; Wallace, G. G.; Mazzoldi, A.; De Rossi, D.; Rinzler, A. G.; Jaschinski, O.; Roth, S.; Kertesz, M., *Science* 284 (1999) 1340.
- [9] R.N. Viswanath, D. Kramer, J. Weissmueller, *Electrochem. Acta.* (under review)
- [10] S. Trasatti, A. Petrii, *Pure & Appl. Chem.*, 63 (1991) 711.
- [11] P. S. Germain, W. G. Pell and B. E. Conway, *Electrochimica Acta* 49 (2004) 1775
- [12] L. Maya., M. Paranthaman, T. Thundat., M. L. Bauer; *J. Vac. Sci. Technol. B*, 14 (1996)15.
- [13] S. Parida, D. Kramer, C. A. Volkert, H. Rösner, J. Erlebacher and J. Weissmüller, *Phys. Rev. Lett.* 97 (2006) 035504.
- [14] B.E. Conway, *Prog. Surf. Sci.* 49 (1995) 331
- [15] Kolb, D. M., *Prog. Surf. Sci.* 51(1996), 109.
- [16] Bach, C. E.; Giesen, M.; Ibach, H.; Einstein, T. L., *Phys. Rev. Lett.* 78 (1997), 4225.
- [17] Erlebacher, J., *J. Electrochem. Soc.*, 151 (2004), C614
- [18] J. M. Dona and J. Gonzalez-Velasco, *J. Phys. Chem.* 97 (1993) 4714
- [19] J. Weissmüller, R.N. Viswanath, D. Kramer, R. Würschum and H. Gleiter, *Science* 300 (2003) 312.

Chapter 7: Summary

The main findings of the research covered in this thesis can be summarized as follows:

The structural and functional properties of nanoporous metals produced by dealloying depend on the pore shape, size and distribution and ligament size and interconnectivity. For the first time, the complete microstructural and topological properties of the nanoporous gold which characterize nanoporous structures, such as specific surface area, pore and ligament size were studied using 3D-electron tomography in a TEM microstructure.

The microstructure of npg shows continuous network of branched ligaments, without having any defined cell or cell wall as is found in a conventional porous material. The microstructure of npg was observed to be quite non-uniform. The diameter of the ligaments varies from less than 5 nm to more than 30 nm. There is a wide distribution in pore sizes. Its microstructure shows existence of small and quite complex pores and almost circular ligament rings of various sizes.

From the 3-D reconstruction, the surface average value of the mean curvature, $\langle\kappa\rangle$, was found to be $55/\mu\text{m}$, which is comparable to the value of $\langle\kappa\rangle$ ($62.5/\mu\text{m}$) calculated for cylindrical ligaments of radius $r = 16$ nm (which is the mean ligament size deduced from the pore size distribution).

Using Silver-gold alloys as a model system the effect of dealloying on sample dimension was studied. For the first time, a macroscopic shrinkage up to 20 vol% was observed during electrochemical dealloying of Ag-Au. Such volume deformation during dealloying was found to depend on the dealloying potential (hence on dissolution

rate) and the composition of the alloy. Addition of incremental amount of Pt in Ag-Au alloy composition reduces the extent of volume shrinkage during dealloying, which could be due to pinning of Au atoms by impurity Pt atoms or due to solid solution hardening.

Comparing X-ray diffraction of Ag-Au alloys, before and after dealloying, shows conservation of original crystal lattice during dealloying. This observation is also corroborated by texture analysis of gold leaf samples before and after dealloying and TEM observation.

The volume shrinkage during dealloying is not consistent with a process exclusively involving dissolution and diffusion on a rigid lattice. Therefore, local plastic deformation processes was suggested as extension of the existing model.

In contrast to recent experimental findings, where the variation of surface stress (f) with charge (q), expressed as surface stress-charge coefficient (ζ), is negative, freshly prepared npg shows a unusual positive ζ . The observation was explained by the presence of adsorbate layer which modifies the nature of the surface and thereby the nature of metal-electrolyte interface. Calculation using reduced charge obtained after cathodic reduction shows a monolayer of oxygen covering the surface of a freshly prepared npg. However, after the cathodic reduction, the sign of ζ is negative, as normally observed. The surface area of the sample found to be reduced by a factor of ten after cathodic cycling and hence the strain amplitude, which may have little influence on the sign of the ζ .

Formation of bulk gold oxide during dealloying or surface reconstruction, can not explain the behaviour of freshly prepared npg. As observed in case of dealloying of Ag-Au alloy, the grain shape and orientation is remain unchanged during dealloying, which is contradictory to the formation of a bulk oxide during dealloying, which will involve change in structural integrity by nucleation of new crystallites. Again, gold surface reconstruct when sufficient negative charge is added to the surface, which may not be a possibility since dealloying is performed at large positive potentials. Ineffective screening due to oxide layer is suggested, which creates a wider space charge layer. Implying that the excess charge is filling the bulk-like unoccupied states, which are antibonding and thereby, giving an unusual positive ζ .

The maximum strain amplitudes obtained in nanoporous Au-Pt alloys are larger by factor of 5-7 as compared to nanoporous gold prepared by dealloying Ag-Au alloys. The electrochemically measured surface area increases with atomic percent of the Pt in the alloy; suggesting a correlation between existence of smaller structure size and enhancement strain amplitude in different nanoporous Au-Pt alloys.

Thus, the studies of dealloying range from understanding the corrosion process to the learning of how to make porous nanomaterials for structural or functional applications. Besides, materials science issues such as lattice defects and plasticity may emerge as new aspects in the field. The information obtained from 3D-TEM study will

contributes to establishing a basic description of the topology and local structure of nanoporous metals prepared by dealloying, which may form the basis for future models leading to a predictive understanding of their properties, such as strength, surface induced strain, or transport properties.